

Fracture Characterization at the Dickman Field, KS: Integrating Well Log and Prestack Seismic Analyses

A Thesis

Presented to

the Faculty of the Department of Earth and Atmospheric Sciences

University of Houston

In Partial Fulfillment

of the Requirements for the Degree

Master of Science

By

Timothy Brown

August 2012

Fracture Characterization at the Dickman Field, KS: Integrating Well Log and Prestack Seismic Analyses

Timothy Preston Brown

APPROVED:

Dr. Christopher L. Liner, Committee Chair, Advisor

Dr. Jolante Van Wijk, Committee Member

Dr. Bernhard Bodmann, Outside Committee
Member

Dr. Mark A. Smith

Dean, College of Natural Sciences and Mathematics

Fracture Characterization at the Dickman Field, KS: Integrating Well Log and Prestack Seismic Analyses

An Abstract of a Thesis

Presented to

the Faculty of the Department of Earth and Atmospheric Sciences

University of Houston

In Partial Fulfillment

of the Requirements for the Degree

Master of Science

By

Timothy Brown

August 2012

Abstract

Dickman Field, located in Ness County, Kansas, has produced 1.7 million barrels of oil since 1962 and is presently being evaluated by the University of Houston as a potential CO₂ sequestration locality. The primary injection target is a porous, brine-saturated, Mississippian carbonate unit set approximately -2000 ft (-610 m) subsea. The objective of this study is to characterize sub-vertical fracture networks that potentially favor mobility of free-state CO₂ within the reservoir.

The 6 Hz results from a narrow-band decomposition of the Dickman 3D broadband volume show NW and NE striking lineaments in the reservoir interval. These spectral anomalies were originally assumed to be evidence of sub-resolution fracturing. Testing the validity of these features was accomplished by analyzing two kinds of data: 1) digital well logs from nearby wells and 2) available prestack seismic data from the Dickman 3D survey. A fuzzy inference system was used to obtain ground-truth fracture information from conventional well logs. Results show probable indicators of crosscutting fractures in the Mississippian section. Prestack analysis was used to detect azimuthal variations in the reflectivity gradient using amplitudes picked from the Gilmore City horizon. Azimuthal anisotropy orientations agree with the 6 Hz features as well as with lineament orientations found in previous seismic attribute studies. The 6 Hz anomalies, although supported by geological and geophysical evidence in terms of orientation, are most-likely products of low-frequency noise found in the upper 0.2 seconds of the Dickman 3D.

Table of Contents

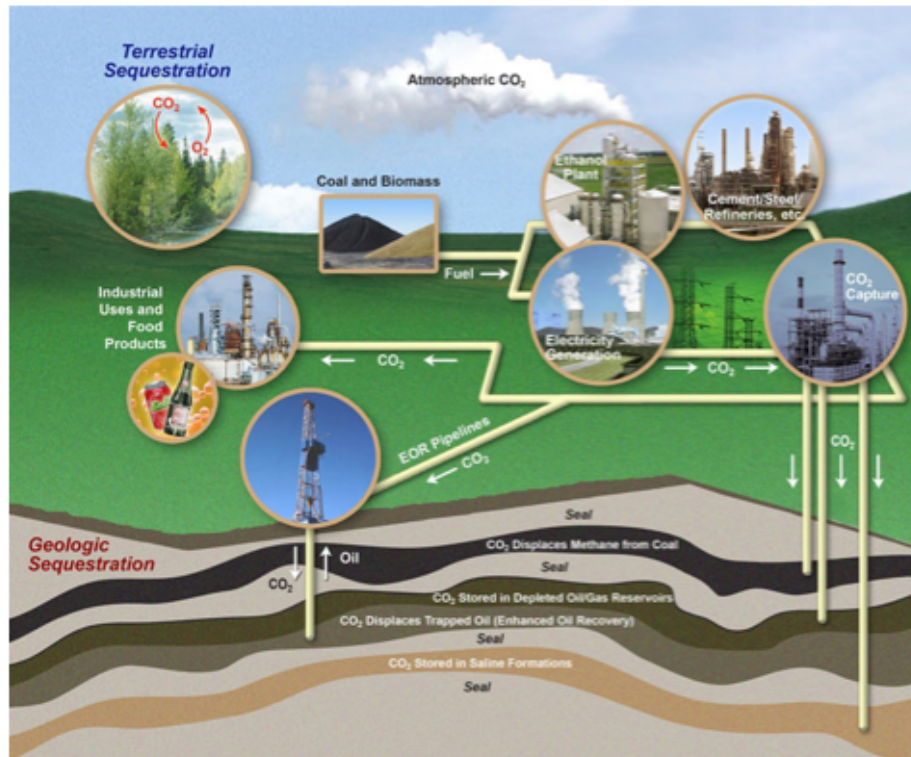
1.0 Introduction	1
2.0 Objectives and Methodology.....	6
3.1 Geologic History	9
3.2 Fracture evidence	15
4.0 Narrow-band Filtering.....	20
5.0 Well Log Analysis.....	31
5.1 Well Log Responses	32
5.2 Fuzzy Set Theory.....	36
5.3 Fuzzy Inference Systems	38
5.4 Case Study	49
6.0 Prestack Analysis	61
6.1 HTI Model.....	62
6.2 AVAZ Theory.....	65
6.3 Data Preparation.....	68
6.4 Results	76
7.0 Discussion	80
8.0 Conclusions.....	83
9.0 Future Work.....	85
References	86
Appendix A	90

1.0 Introduction

The global warming issue has catalyzed environmental reform concerning the need to reduce anthropogenic carbon dioxide (CO₂) in the Earth's atmosphere. Carbon capture and storage programs (CCS) seek to reduce this effect by targeting fossil-fuel power plants because of their high CO₂ emission rates (Global CCS Institute, 2011). In the CCS process, the CO₂ byproduct is captured and compressed, then transported and injected into a geological formation (Figure 1). CCS sites are deemed reliable based on their ability to retain the post-injected CO₂. Preferentially oriented fracture networks and other permeable mechanisms affecting a reservoir's seal provide conduits that may lead to the contamination of near-surface aquifers and other resources meant for human consumption. As a result, CCS programs are investigating depleted oil and gas reservoirs (one of six different storage scenarios) for potential injection sites because of their abundance and proven seal integrity (Nissen et al., 2009).

Depleted petroleum reservoirs across the central United States have received significant attention for CO₂ sequestration (Global CCS Institute, 2011). The central U.S. contains the Western Interior Plains aquifer system (WIP), which is an ideal injection target. WIP may be an optimal target because the Mississippian-age, saline aquifer component has a low fluid migration rate (approx. 1 cm/year) and reservoir properties that boost CO₂ solubility (Jorgensen et al., 1993; Carr et al., 2005). However, since CCS programs expensive and pose a potential public safety risk, characterization is required before any site is proven feasible.

(a)



(b)

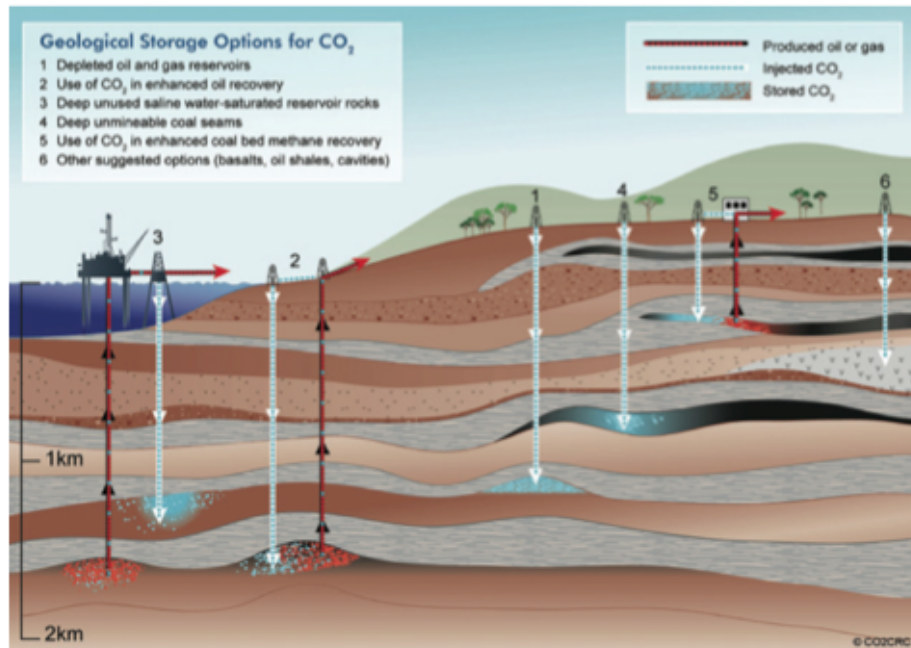


Figure 1: (a) Illustrated example of the CO₂ sequestration process includes natural and industrial processes (Plasynski et al., 2007). (b) Illustrated example of different geological storage options for anthropogenic CO₂ sequestration (Global CCS Institute, 2011).

The Dickman Field, located in Ness County, Kansas, has produced 1.7 million barrels of oil from porous shelf carbonates since 1962 and is presently being evaluated as a potential CO₂ sequestration locality (Liner et al., 2010) (Figure 2). The collective goals are to understand the relevant CO₂ trapping mechanisms and ultimately model the free gas flow in the reservoir following decades of CO₂ injection. There are two proposed injection targets in the Mississippian section. The primary target is an aquifer unit located approximately -2000 ft (-610 m) subsea and the secondary is the overlying oil reservoir. These depths provide optimal pressure and temperature conditions permitting super-critical behavior of the injected CO₂, thus allowing a portion to dissolve in the reservoir fluids (Davidson et al., 2005). The remaining CO₂ will either be immobile, trapped in porous media or in a free gas state contingent on structural trapping for retainment (Davidson et al., 2005) (Figure 3). This thesis takes a geophysical approach toward characterizing sub-vertical fracture networks that potentially favor mobility of the free-state CO₂ within the Mississippian target zones.

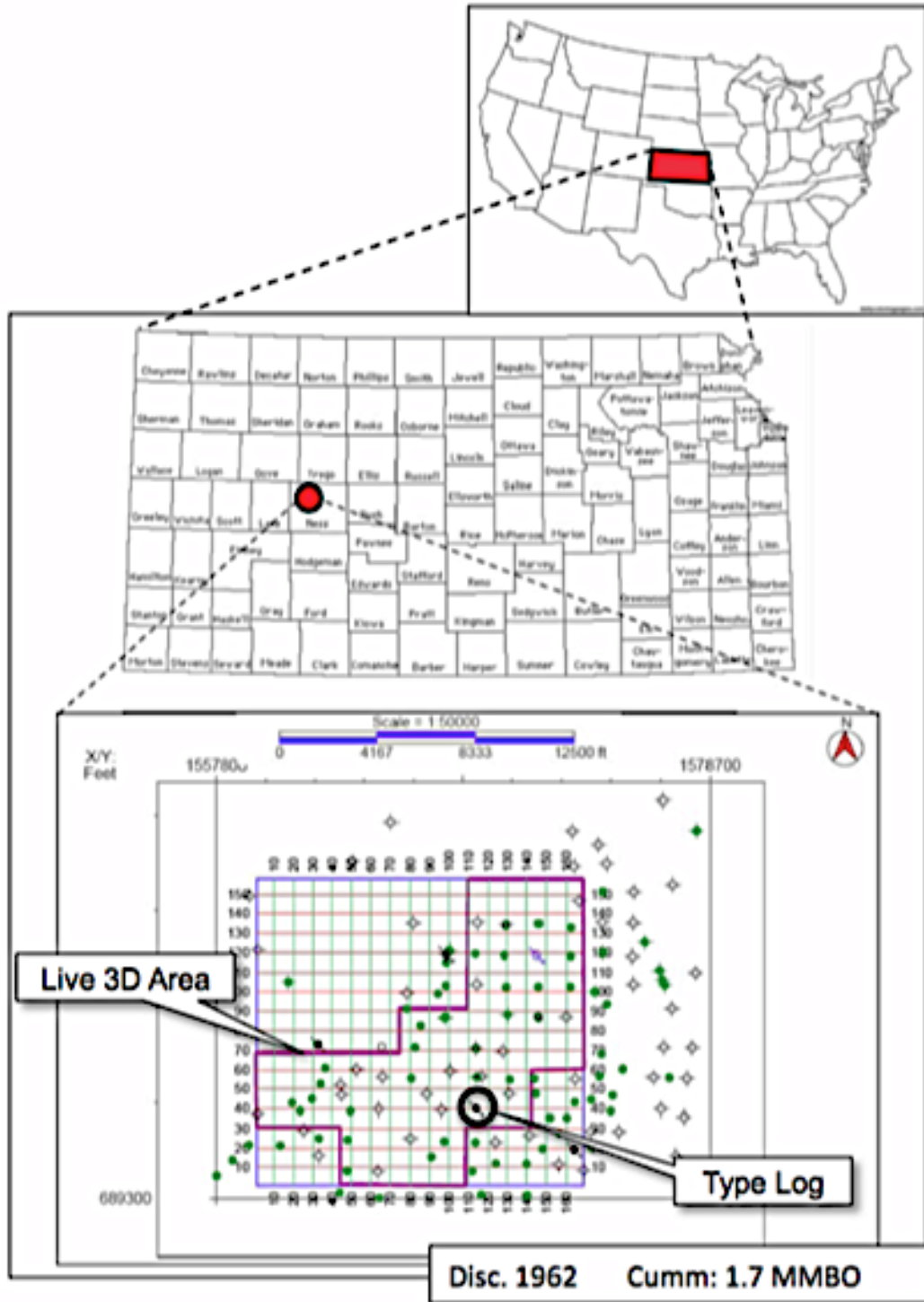


Figure 2: Geographical location of the Dickman field. The live 3D seismic coverage and local well proximities are shown on the bottom figure. From Liner et al. (2010).

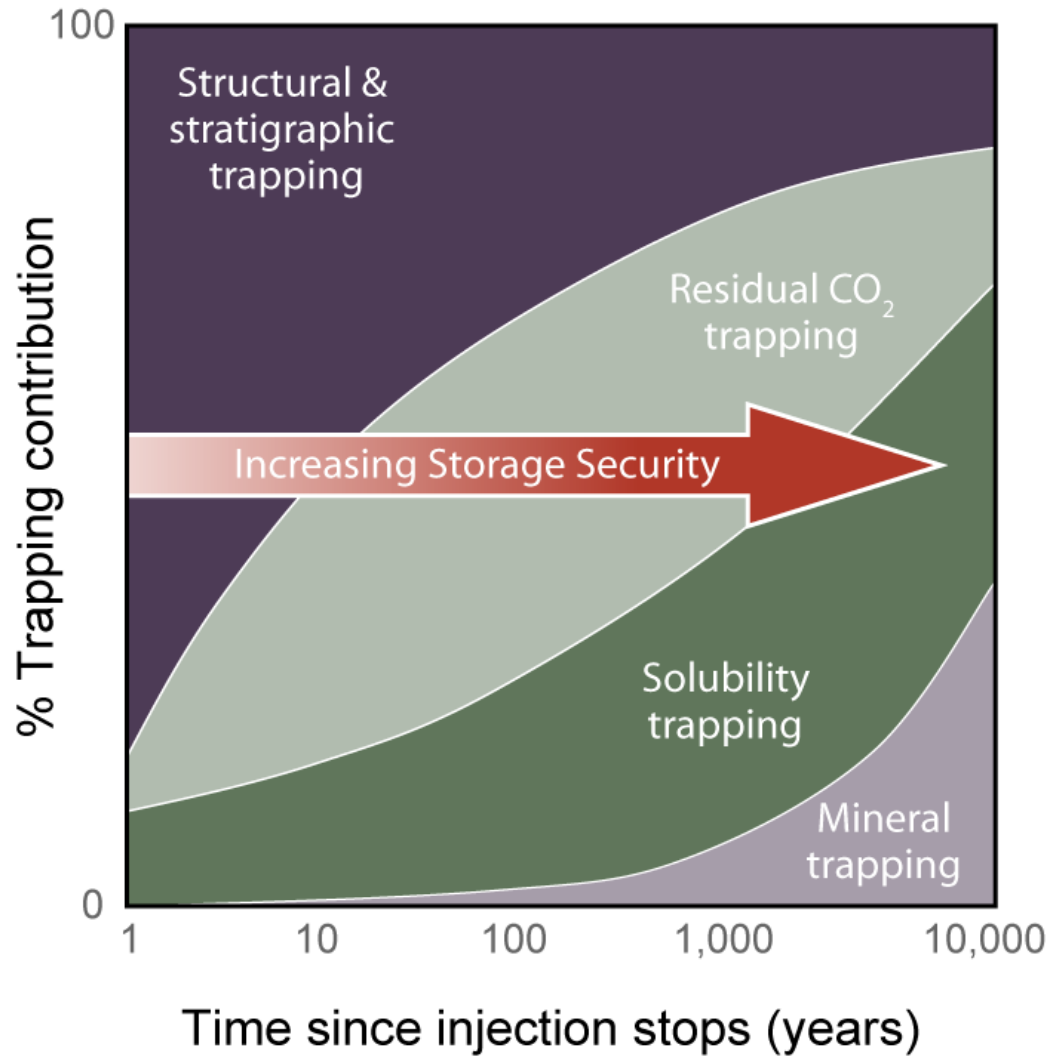


Figure 3: Diagram showing the contributions of the CO₂ trapping mechanisms as a function of time. Initial storage security depends on structural and stratigraphic trapping. As time progresses, the dependency shifts to more secure mechanisms such as solubility trapping and mineral trapping. From Davidson et al. (2005).

2.0 Objectives and Methodology

In the petroleum industry, 3D seismic data is routinely acquired for exploration and reservoir development. Geophysicists typically use seismic attributes, prestack inversion methods, and full-wave sonic logs to determine principle stress orientations and identify local fracture trends. Moreover, supplements such as conventional well logs and core data also provide evidence of fracturing in the reservoir. This geomechanical information optimizes well placement and completion strategies ultimately increasing hydrocarbon productivity. The focus of this study is to use similar data to find dominant fracture trends, if any, that enable migration of post-injected CO₂.

Seismic attributes extracted from the Dickman 3D show potential evidence of sub-resolution fracturing at the reservoir and aquifer levels (Nissen et al., 2009). Moreover, results from a 6 Hz isolation of the broadband volume show linear anomalies potentially related to the same trend (Figure 4). This thesis seeks to determine whether these features are responses from sub-resolution fracturing, or related to acquisition footprint or processing artifacts. Azimuthal AVO (Amplitude Variation with Offset) and fracture indicators from conventional well logs are used to obtain fracture information that may validate previous interpretations. The combined results will be used to test the hypothesis that low frequency seismic features indicate natural fractures, and therefore give information on reservoir and seal structural integrity.

It is important to note that the majority of CCS research concerning depleted petroleum reservoir depends on data obtained during exploration and development of that particular reservoir. Consequently, available geophysical or geological data may not be ideal when working towards a specific objective. As an additional goal, this research hopes to inform the CCS community on what can be accomplished with old or limited geophysical/geological data sets.

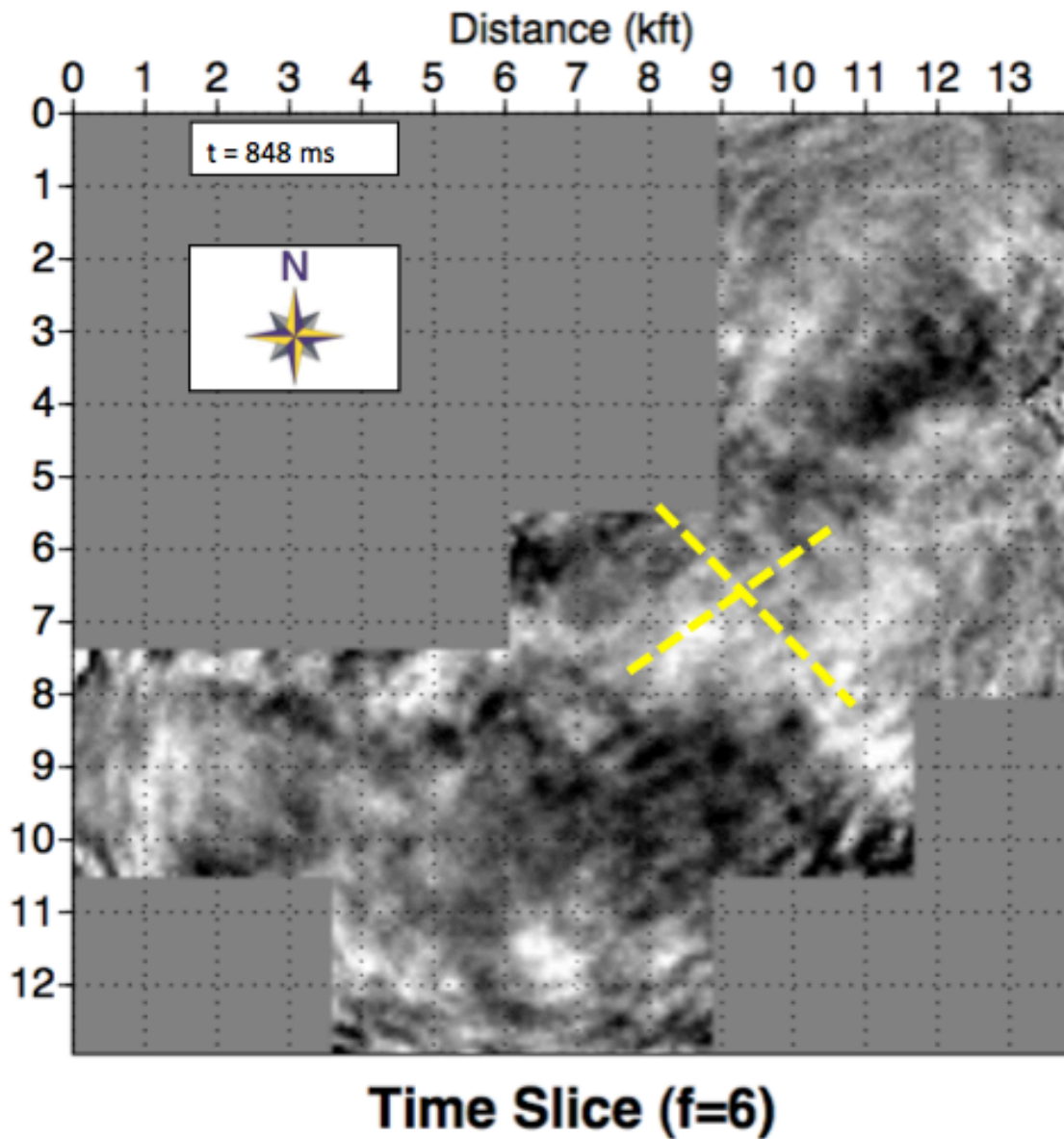


Figure 4: 6 Hz time slice representing the Mississippian-Pennsylvanian unconformity surface. Notice the prominent NE-NW trending features in the center of the survey. The working hypothesis is that these features emanate from natural fracturing in this subsurface interval. Modified from Seales et al. (2011).

3.0 Background

3.1 Geologic History

The Central Kansas portion of the WIP aquifer system is divided into two members: a lower member of Cambrian sandstone and Cambro-Ordovician carbonates, and an upper member of Mississippian carbonates (Figure 5). Lower porosity carbonates and shale separate these aquifer units. This thesis focuses on the upper aquifer member as well as the proximal, underlying Mississippian and Ordovician units. The Mississippian aquifer unit consists of Osagean, Meramecian, and Chesterian age, solution-enhanced limestone and dolomites. Kinderhookian age, low porosity shelf carbonates underlay the aquifer, while cyclical Pennsylvanian limestone and shale deposits unconformably overlay the reservoir, collectively acting as the confining unit.

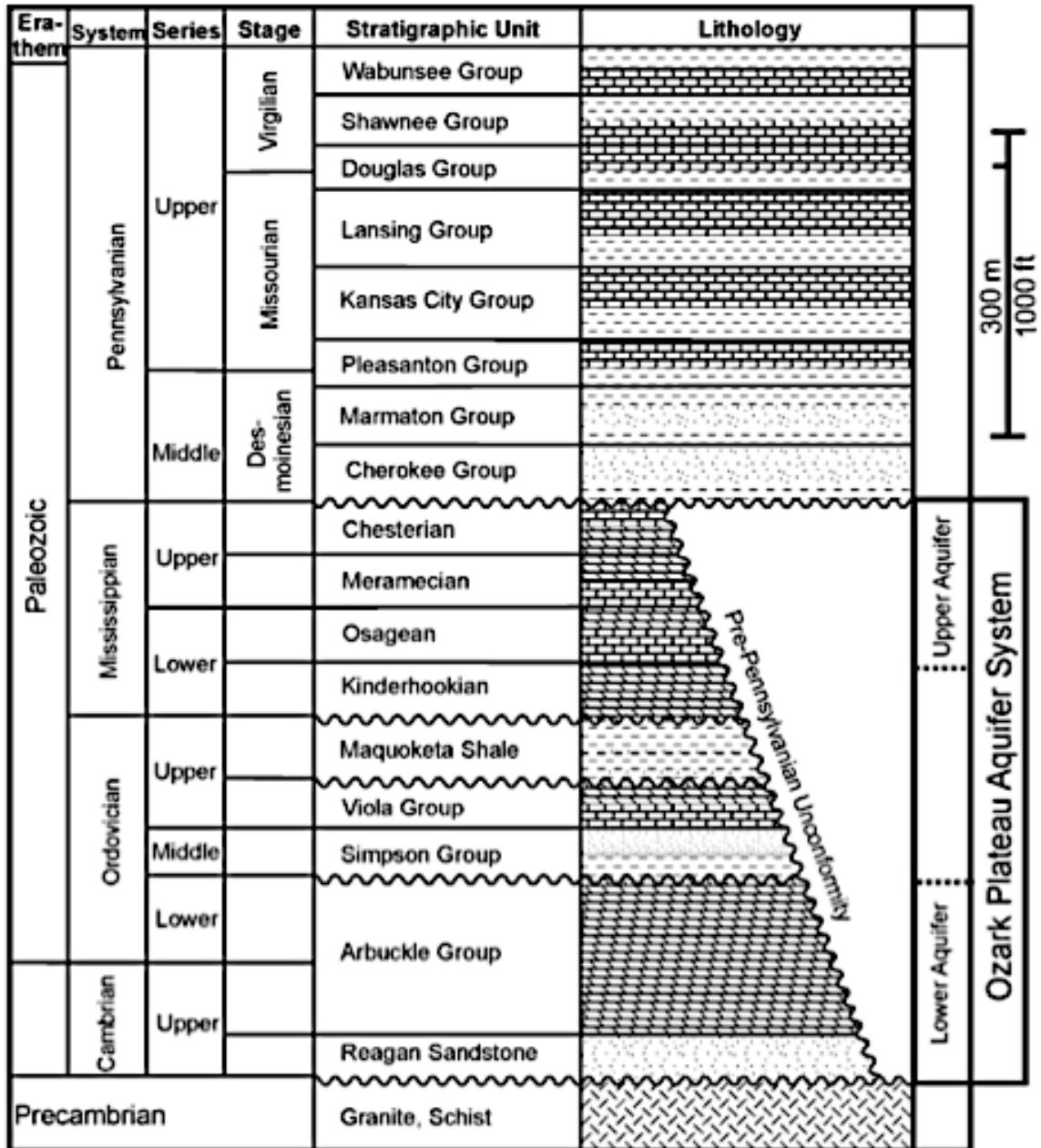


Figure 5: Generalized stratigraphic section of central Kansas showing the configuration of the Ozark Plateau Aquifer System. The focus of this study is the Upper Aquifer component. From Carr et al. (2005).

During the Central Kansas Uplift (CKU), surficial-fluid-driven fracturing and subsequent karsting post-diagenetically enhanced the porosity and permeability of sub-aerially exposed pre-Pennsylvanian strata (Franseen et al., 1998). The CKU,

occurring 335 Ma to 310 Ma, describes a post-Mississippian deformation event following the southward continental collision between Laurussia and Gondwana (Figure 6). A northwest-trending anticline structurally characterizes the CKU. This deformational relic acts as the depositional surface for ensuing Pennsylvanian deposits naturally creating an angular unconformity between older Paleozoic strata.

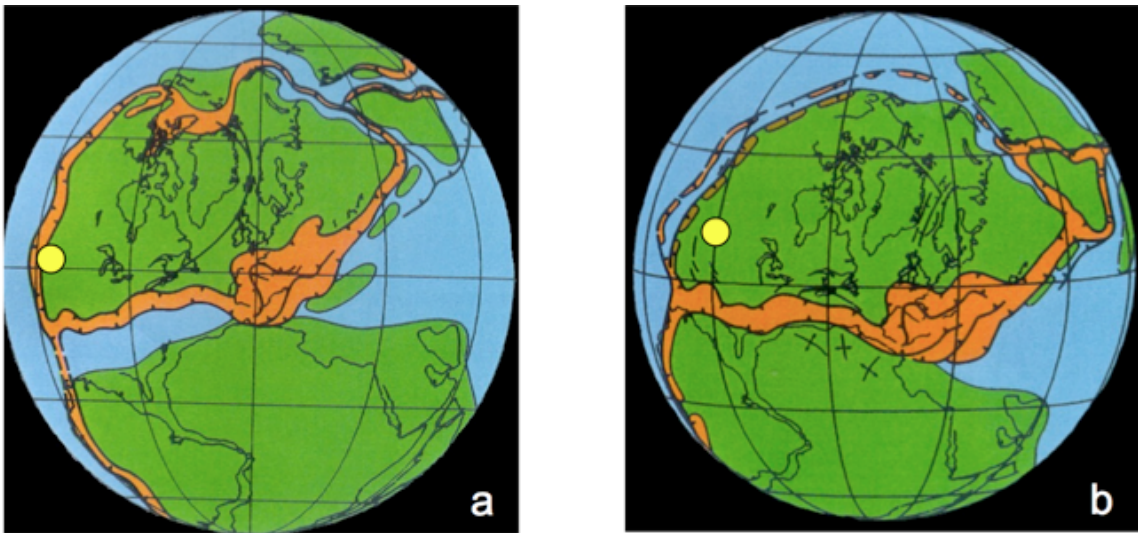


Figure 6: Tectonic configuration of the Laurussia (North) and Gondwana (South) at a) 335 Ma (Mississippian) and b) 310 Ma (Pennsylvanian). The Yellow dot marks the relative location of the study area. Modified from Ziegler (1989).

Dickman Field is located on the western limb of a northwest-trending anticline (Figure 7). A type log from Stiawalt 3 describes the stratigraphy (Figure 8). The Mississippian interval consists of solution-enhanced limestone and dolomites underlain by low porosity Kinderhookian shelf-carbonates. At Dickman, the Pre-Desmoinesian exhumation of Upper-Mississippian strata removed Chesterian strata leaving only the Meramecian and Osagean aquifer components (Nissen et al., 2009).

Incised channel deposits of the Lower-Cherokee group, associated with post-Mississippian uplift and erosion, extend through the Upper-Mississippian carbonates and marks the Mississippian-Pennsylvanian unconformity boundary. The following geological events chronologically summarize the stratigraphy and structural history of the units of interest at the Dickman field (Liner et al., 2010):

- 1) Short-term Gilmore City (GMC) exposure initiating karst development.
- 2) Unconformable deposition of Osage shelf limestone and dolomite facies on GMC; lithofacies spatially affect primary porosity and subsequent secondary porosity distribution.
- 3) Cyclical exposure of younger Mississippian units (Warsaw-Salem) leading to solution enhanced fracturing of older units and subsequent karst development.
- 4) Post-Mississippian, long-term exposure and erosion of Salem/Warsaw, attributed to the tectonic evolution of the Central Kansas Uplift, initiating faulting, fracturing, expansive karsting, and sub-surface dissolution.
- 5) Deposition of Pennsylvanian strata
- 6) Post-Pennsylvanian folding and fracturing creating a dominant NE structural fabric.

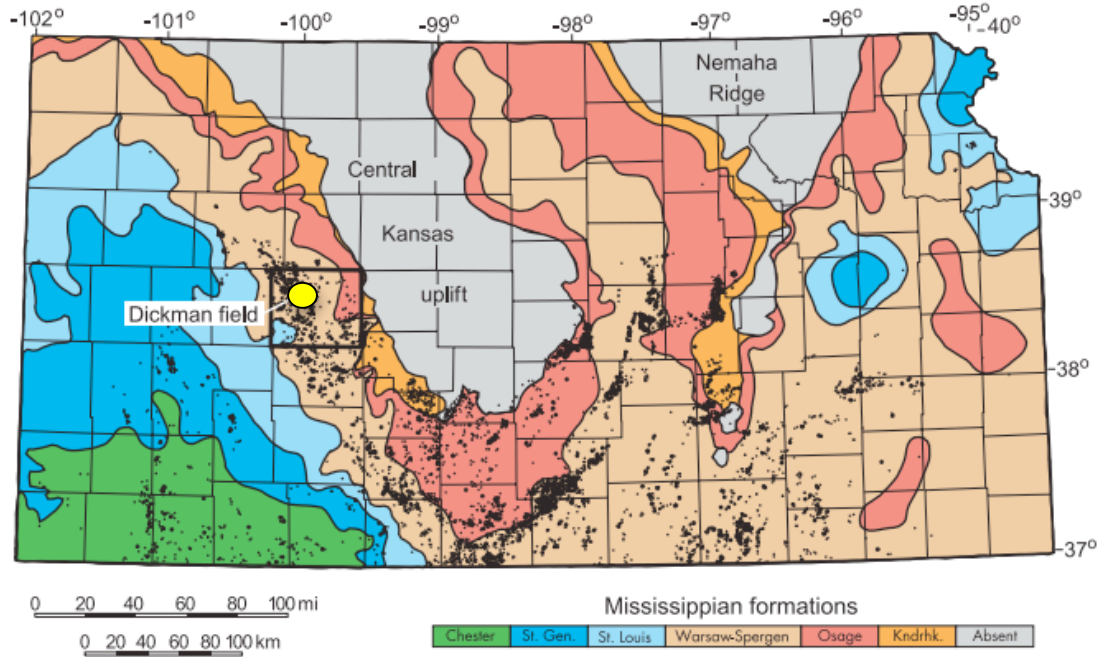


Figure 7: Subcrop map of Mississippian units in Kansas. The structural orientation of the anticline is NW-SE. The black marks indicate locations of producing or past-producing petroleum fields. Dickman Field lies on the western flank of the CKU. Modified from Nissen et al. (2009).

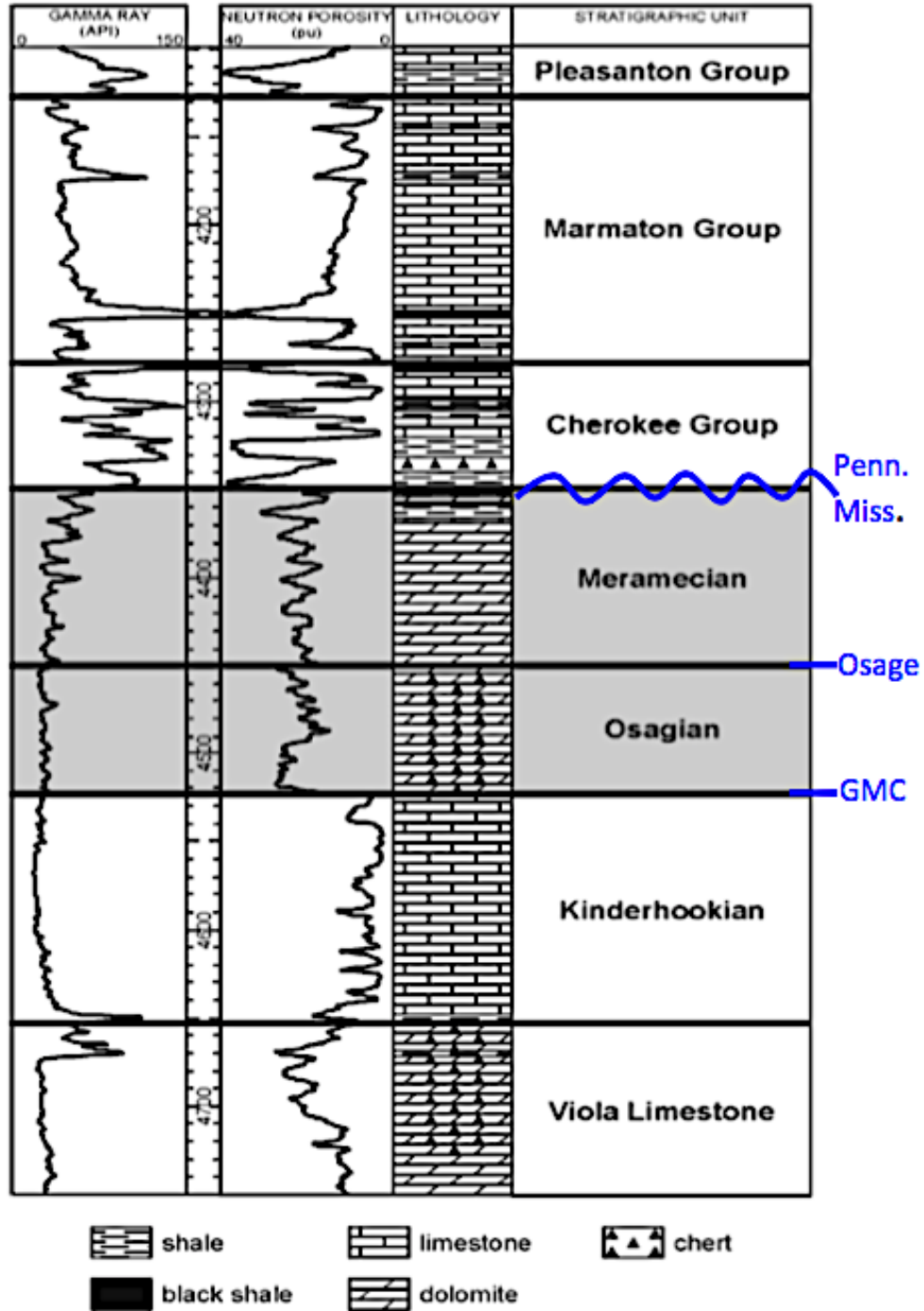


Figure 8: Stiwalt 3 type log. The depth scale is measured depth (MD) in ft. The log shows the relevant stratigraphic units and corresponding rock types. The interval shaded in gray represents the reservoir and aquifer components. Notice that the reservoir consists of porous carbonates confined by a cyclical shale/carbonate sequence above (Cherokee) and a low-porosity carbonate below (Kinderhookian). Key formations include the Osage and the Gilmore City (GMC). Modified from Nissen et al. (2009).

3.2 Fracture evidence

The term “fracture” in this work describes any surface along which a rock has lost cohesion. Features such as faults, joints, micro-cracks, and disconnected bedding surfaces are categorized as fractures. Joints are a type of fracture with relatively little or no displacement along its surface, while faults have significant shear-type displacement within a zone or along a planar surface (Twiss and Moores, 2006). Fractures form in response to body forces (force due to gravity) or surface forces (tectonic forces), and depending on the observational scale, fracture geometry can vary locally or extend regionally. Tectonic fractures form in response to surface forces, which correspond to a tectonic event. They often have complex geometries, dynamically change over a relatively small scale, and form in relation to major structures such as faults and folds (Nelson, 2001). Regional fractures form in response to body forces in a systematic way, usually as orthogonal pairs perpendicular to bedding. They usually reflect basin geometry, show minimal displacement, and have relatively consistent geometries over a regional scale (Nelson, 2001). Mississippian rocks in Central Kansas are believed to exhibit both these fracture types (Merriam, 1963).

Fracturing has been either interpreted or identified at various scales in Central Kansas. A map of the Central United States shows that the majority of structural features north of the Ouachita Orogeny have either a NE-SW or NW-SE orientation (Figure 9). Smaller scale features local to these major structures are likely to share the orientations. In addition, Nissen et al. (2009) interprets sub-

vertical fracture sets in the Mississippian reservoir from geophysical data acquired at the Dickman Field (Figure 10). The results show a consistent bi-directional trend: NE-SW and NW-SE. It is important to note that the curvature volumes show evidence of a possible sub-resolution fracturing trend, which agrees with the orientations of the 6 Hz anomalies from Figure 4. Furthermore, clastic-filled vertical fractures crosscut horizontal wells adjacent to the Dickman Field (Carr et al., 2000). These fractures have widths up to 5 ft (1.5 m) and are filled with debris from eroded Upper Mississippian rock and encroaching Pennsylvanian deposits, demonstrating evidence of enhanced dissolution of Upper Mississippian strata during the CKU (Carr et al., 2000). Moreover, Figure 11 shows core photos taken from surrounding Dickman wellbores. The photos clearly show evidence of sub-vertical fracturing in the Upper Mississippian section.

The general consensus from past studies is that there are two dominant reservoir fracture trends in the greater Dickman area: an open northwest striking set and a healed, or sediment filled northeast striking set that crosscuts the former and impedes fluid movement throughout the reservoir. While past studies provide fracturing evidence from surrounding well control, geophysical methods have yet to provide a clear representation of fracture geometry within the Mississippian reservoir at the Dickman Field.

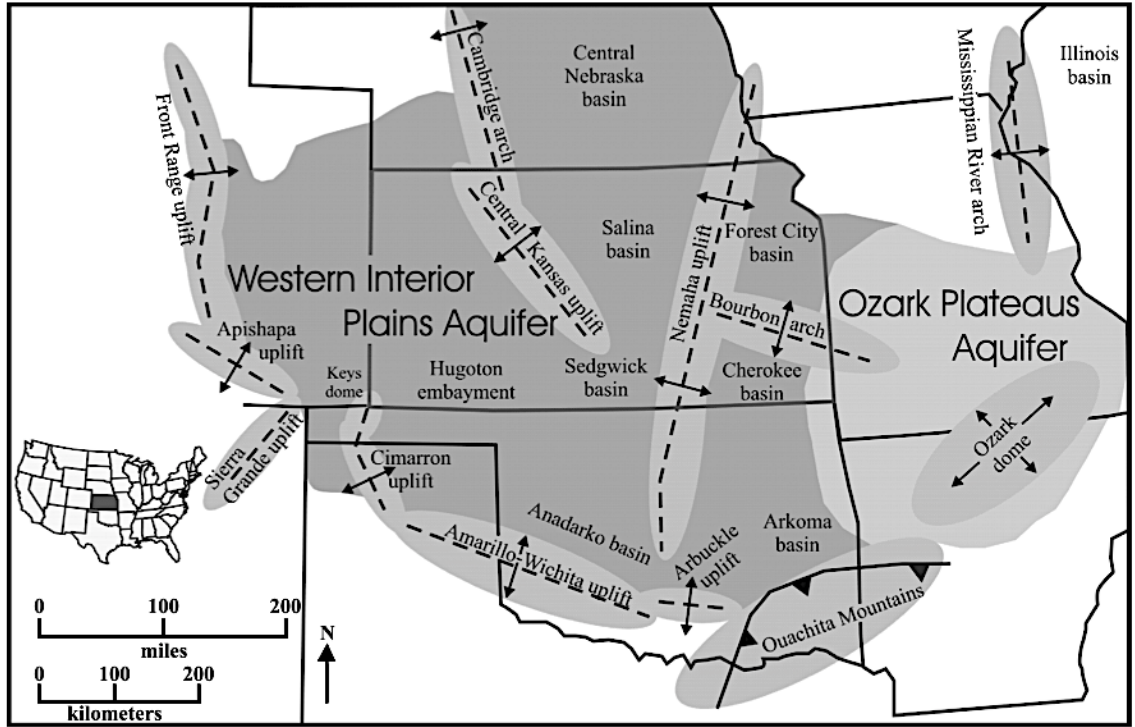


Figure 9: Map of Kansas showing the WIP aquifer system and regional structures of the Central United States Notice the large-scale NW and NE trending features throughout the region. From Carr et al. (2005).

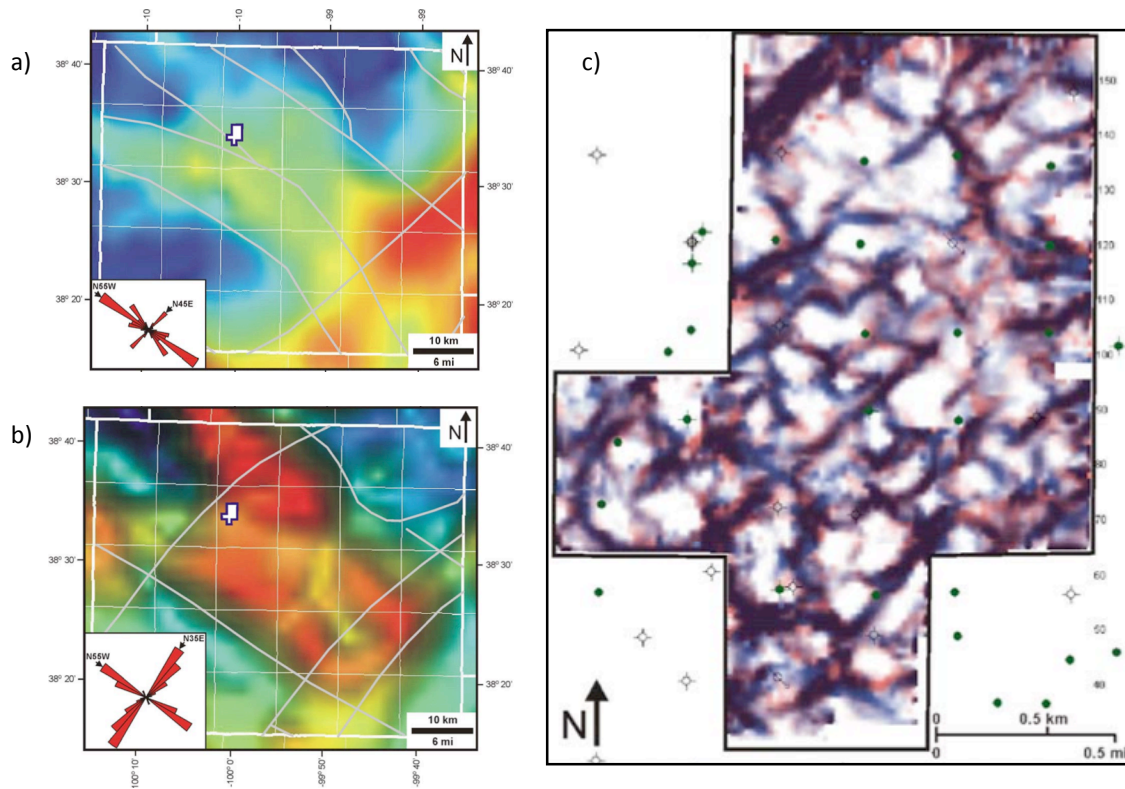


Figure 10: Bouguer gravity map of Ness County, KS (a) (From Kruger, 1997), Aeromagnetic map of Ness County (b) (From Kruger, 1997), and superimposed volumetric most-negative curvature maps of Mississippian horizons extracted from the Dickman 3D. Note the dominant NW-NE oriented features common in all three figures. Modified from Nissen et al. (2009).

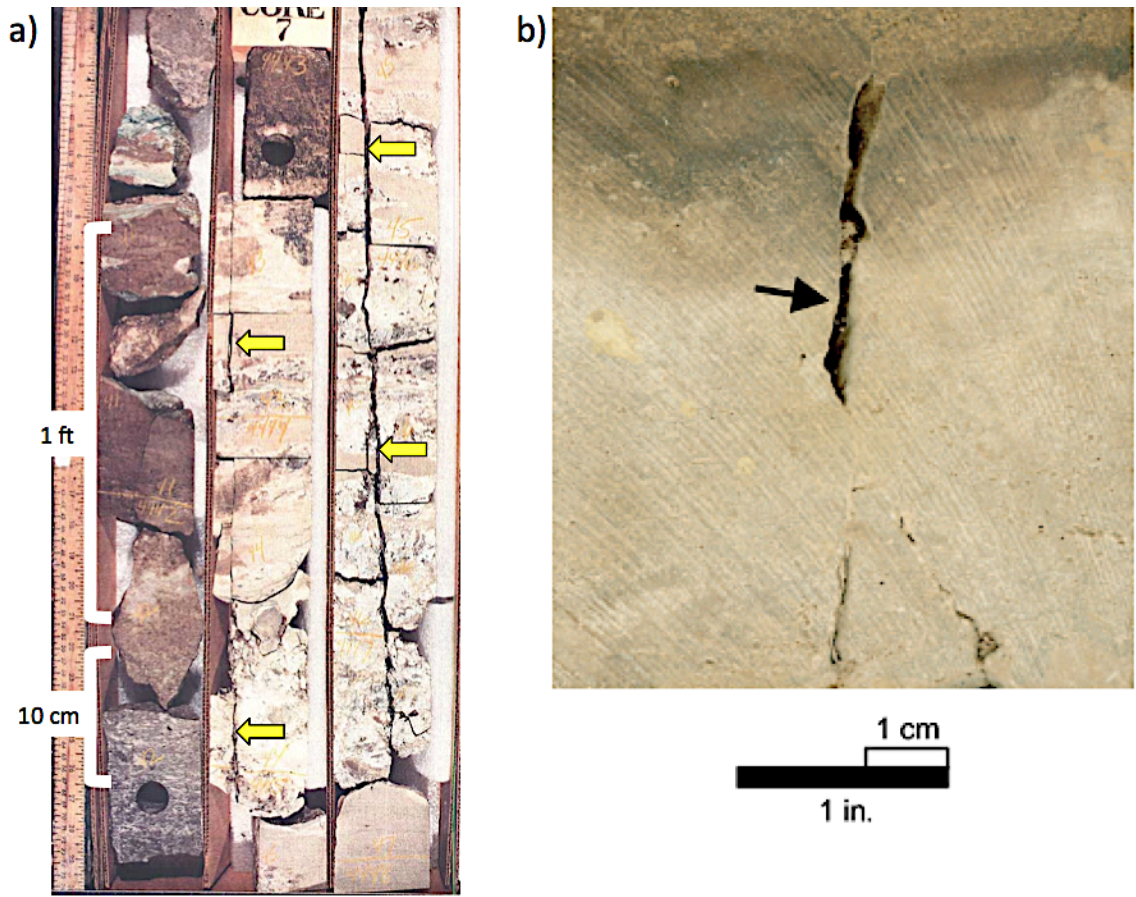


Figure 11: Core photos from (a) Schaben Field well covering an 8 ft (2.4 m) section in the Osage and (b) the Tilley 2 well near the top of the Mississippian. Note the sub-vertical fracture in the right-most column of (a), which is marked by arrows. The fracture is continuous up section (Middle column). Figure 11b shows a solution-enhanced vertical fractured (Nissen et al., 2009).

4.0 Narrow-band Filtering

The Mississippian-Pennsylvanian unconformity is represented in the Dickman 3D seismic data at roughly 848 ms. Producing a time slice through the full bandwidth volume at 848 ms exposes prominent features (Figure 12). The most notable is an incised channel, which represents Lower-Cherokee deposits. Moreover, other features include a northeast-trending fault at the northern edge of the survey as well as evidence of karsting southwest of the channel. However, with exception to the fault, the broadband volume does not provide evidence of linear fracture trends at or near the unconformity boundary.

The 6 Hz narrow-band image created by Seales et al. (2011, Figure 4) provides “visual” evidence of natural fracturing in the Mississippian reservoir. Since this association primarily reflects the interpretation offered by Nissen et al. (2009), who hypothesized that curvature lineaments with similar orientations are indicators of natural fracturing, it is important to understand the procedure going into the generation of this narrow-band image.

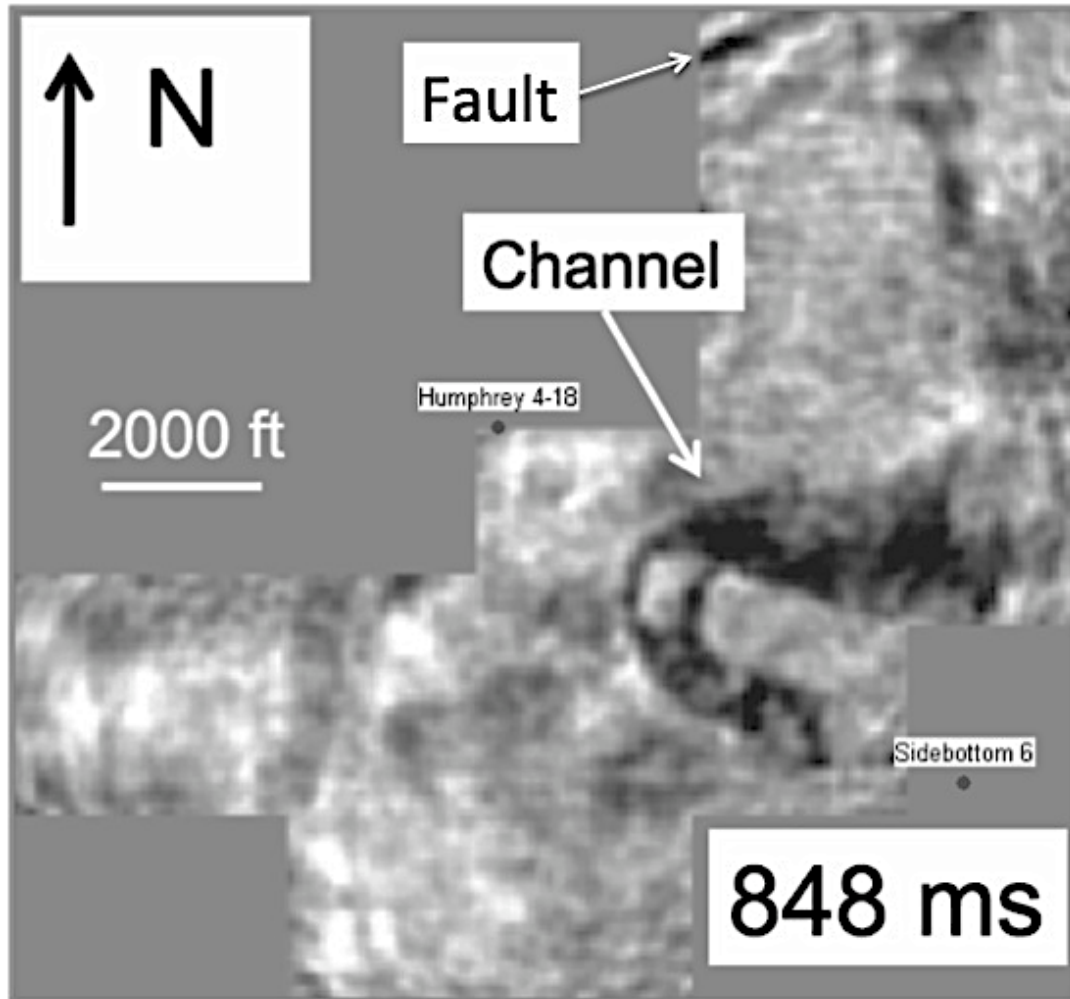


Figure 12: Broadband time slice from the Dickman 3D approximating the Mississippian-Pennsylvanian unconformity. The most notable feature is an incised channel, which represents Lower-Cherokee deposits; other features include a northeast-trending fault at the northern edge of the survey as well as evidence of karsting southwest of the channel.

Various processing stages use zero-phase frequency filtering to extract specific information from seismic data. Figure 13 describes zero-phase frequency filtering. The filter is defined by a band-limited, zero-phase wavelet that, when applied, preserves frequencies from the input trace within the spectrum of the wavelet. The operation in the frequency, or Fourier domain, is the multiplication of a trace's amplitude spectrum with that of the filter. Then, applying the inverse Fourier

transform recovers the filtered time-series. On the other hand, the operation in the time domain is a convolution of the filter's coefficients, which are the time samples of the wavelet, with the seismic trace. The filtered time-series should be the same regardless of the calculation domain. Most importantly, applying the filter only minimally affects the phase spectrum of the input time-series since the filter is zero-phase.

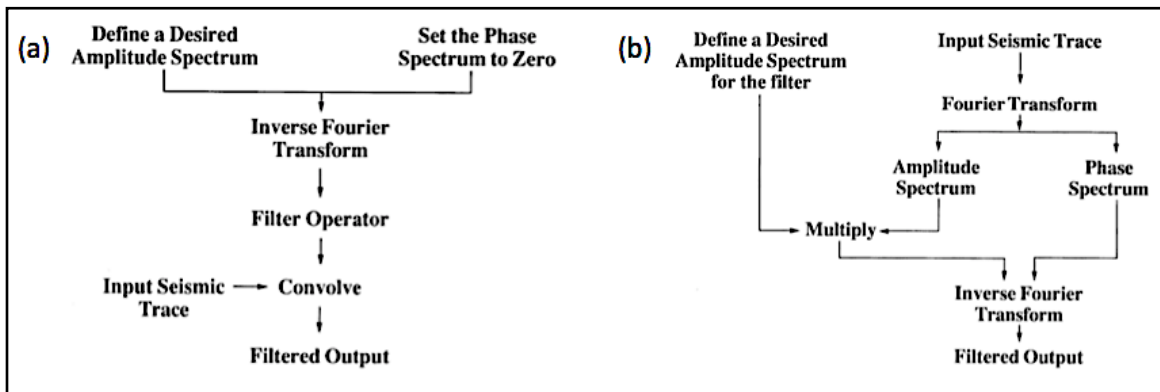


Figure 13: 1D frequency filtering procedure in (a) the Fourier domain and (b) the time domain. Modified from Yilmaz (2001).

Zero-phase frequency filtering is applied to the Dickman 3D (poststack) dataset with intentions of uncovering interference effects related to Mississippian geology. Narrow-band images were created using SUFILTER, a frequency-domain filtering program accessible in Seismic UNIX (SU) (Cohen and Stockwell, 2012). Figure 14 gives an example of a narrow-band spectrum. A filter of this type is translated across the survey spectrum resulting in a collection of narrow-band volumes, which are then interpreted.

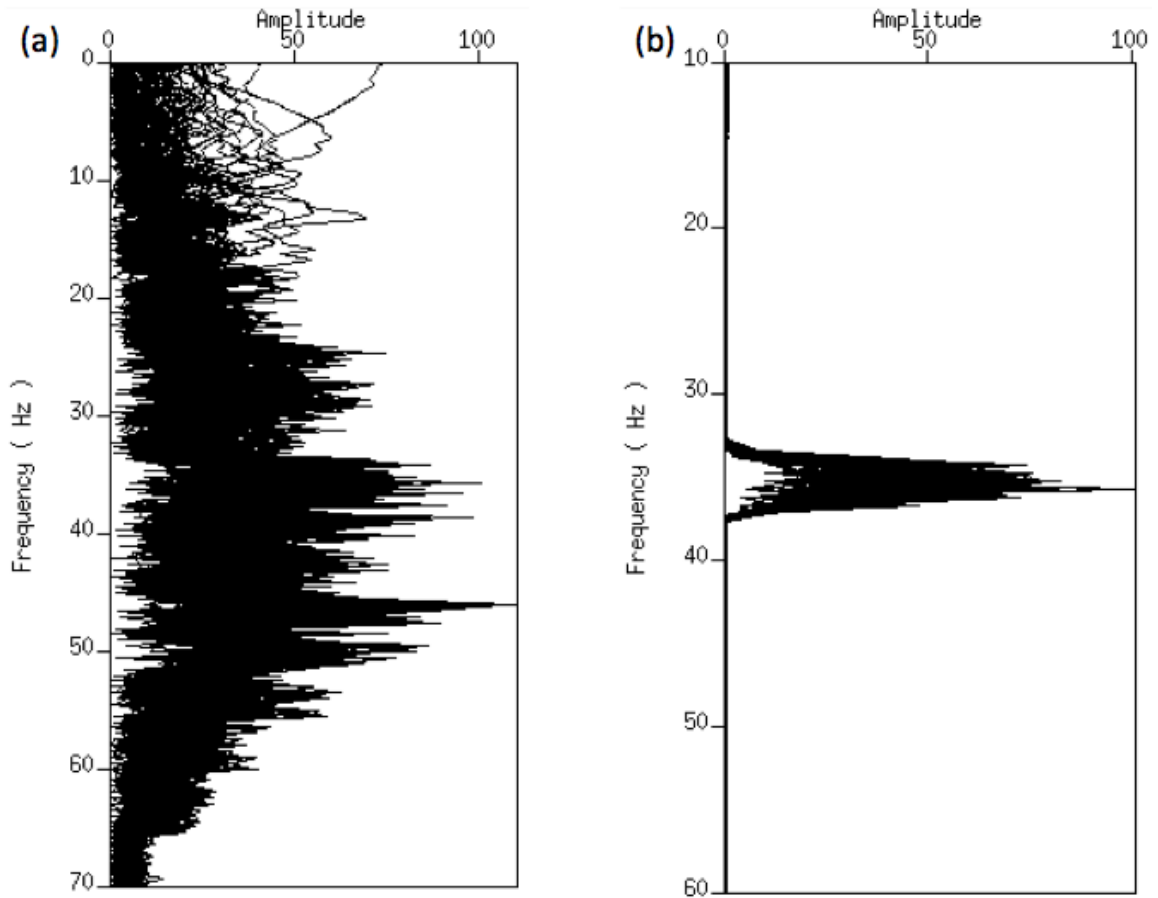


Figure 14: Amplitude spectrum of a random line (a) before and (b) after applying a narrow-band filter centered on 35 Hz. Corner frequencies of the filter are 33-34-36-37 Hz. Note that amplitudes are only preserved in the bandwidth of the filter.

The 6 Hz results are shown again in Figure 15 (formally Figure 4). The image shows prominent northwest-and northeast (NW-NE)-striking lineaments near the center of the survey otherwise absent from the broadband image. These low frequency anomalies appear around 848 ms and are fairly continuous through greater times. This interval spans the Mississippian-Pennsylvanian unconformity through the Lower-Mississippian and Ordovician sections and perhaps indicates regional or fold-related fracturing attributed to post-Mississippian deformation. The

NE-striking lineaments show better continuity and appear to crosscut the NW trend. Nissen et al. (2009) also observes this asynchronous relationship between the two sets.

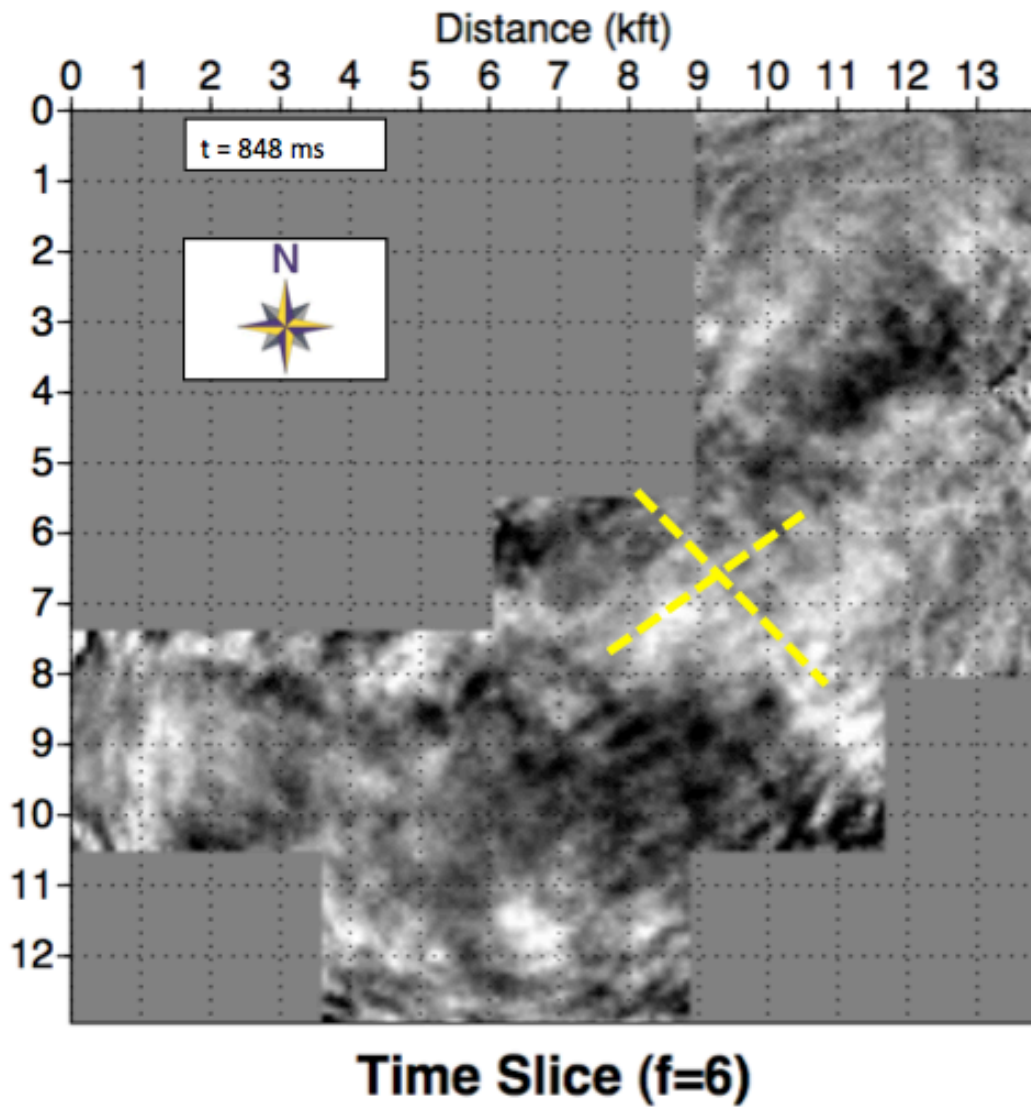


Figure 15: 6 Hz time slice resulting from the narrow-band filtering procedure. The slice represents the Mississippian-Pennsylvanian unconformity surface. Notice the prominent NE- and NW-trending features in the center of the survey. The working hypothesis is that these features emanate from natural fracturing in this subsurface interval. Modified from Seales et al. (2011).

Due to the exceedingly linear nature of these low-frequency features, a natural inclination is to consider effects from acquisition geometry. An acquisition footprint appears in seismic data as an arrangement of lineaments corresponding to the source and receiver geometry and is unrelated to subsurface geology. However, since the Dickman 3D is dominated by an east-west receiver arrangement and an irregular north-south shot arrangement, it is likely that observable effects from the acquisition geometry are not related to the NE-NW features (Figure 16). A 41 Hz time slice of the Dickman 3D (Figure 17) demonstrates the frequency dependence of the inherent acquisition footprint. The image shows prominent east-west-oriented lineaments throughout the survey, which are easily associated with the receiver geometry. However, the acquisition footprint is not always attributed to the receiver geometry or the direction of acquisition. Non-geological amplitude anomalies may arise from an unbalanced azimuth-offset distribution in the prestack gathers (Liu et al., 2011).

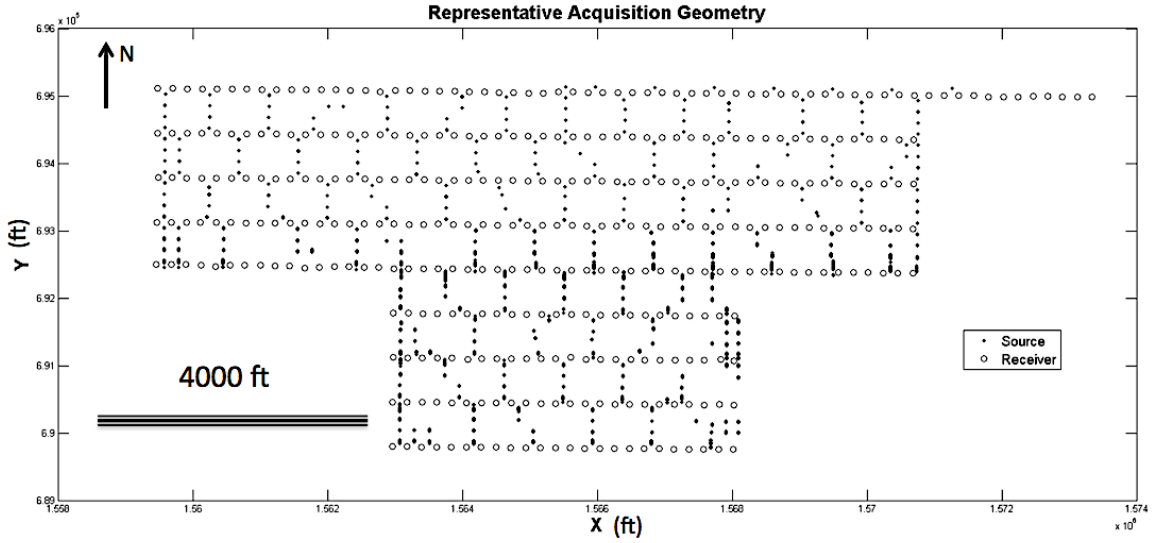


Figure 16: Representative acquisition geometry of the Dickman survey calculated from the prestack headers. The receiver lines have an east-west orientation while the shot lines are predominately north south creating an irregular grid. Notice that these orientations do not agree with those of the 6 Hz anomalies in Figure 15.

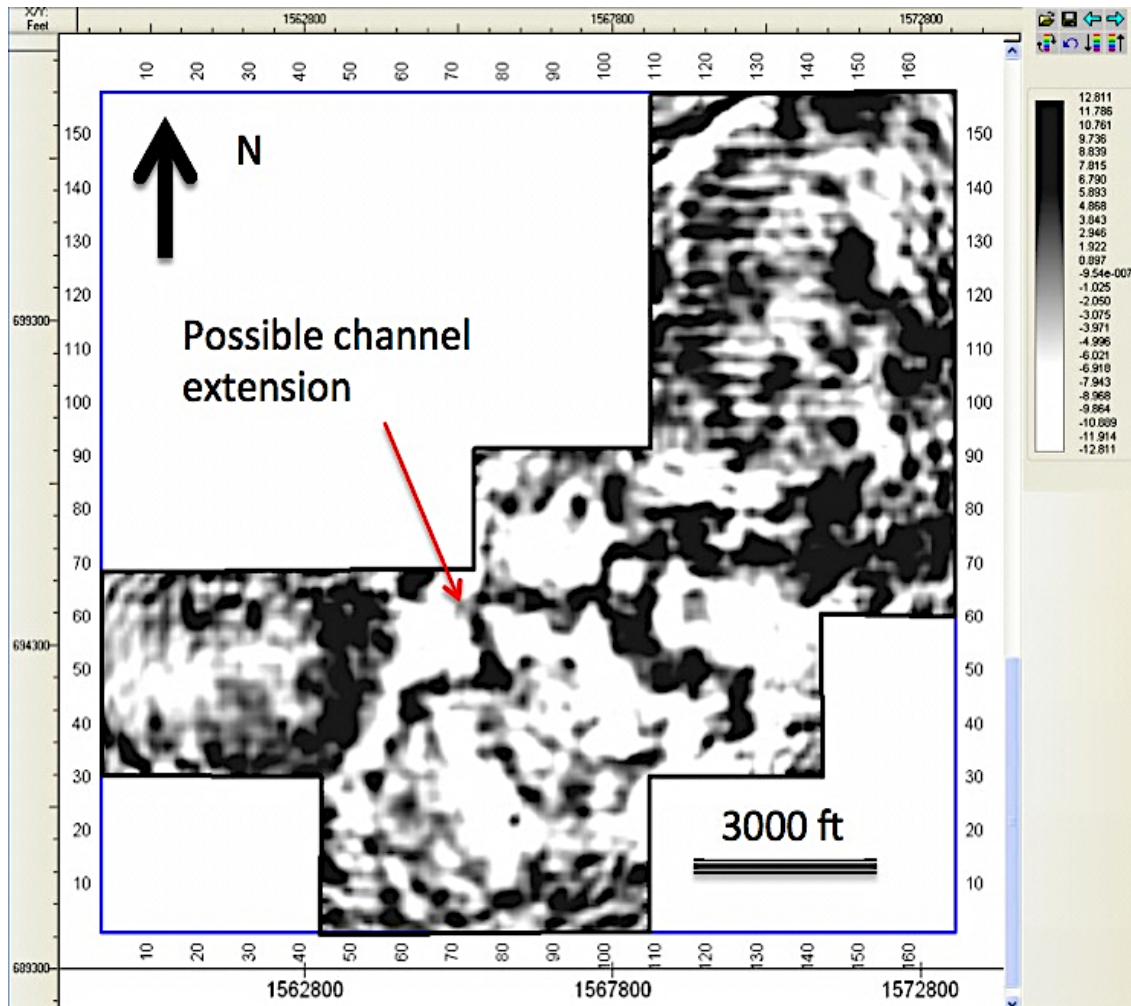


Figure 17: A 41 Hz time slice at 848 ms. Notice the E-W-trending features at the northern end of survey. These frequency dependent anomalies are related to the acquisition footprint associated with the receiver geometry. Also evident is a possible channel extension just west of the main channel. Modified from Seales et al. (2011).

Interpreting the narrow-band results is not intuitive. Although there is some amplitude modulation with respect to time, bandpass filtering over the entire length of a trace assumes interference effects from randomly sampled geology and, therefore, does not consider a time-frequency tradeoff compared to other spectral decomposition methods (Partyka et al., 1999; Castagna et al., 2003; Puryear et al., in press). Furthermore, depending on the natural frequency of the geophones, the low

frequency energy may be associated with noise rather than true signal. Even though Dickman's amplitude spectrum indicates plausible signal at 6 Hz (Figure 14), the corresponding narrow-band image could be accenting low-frequency noise acquired during processing. Moreover, the narrow bandwidth of the filter creates amplitude effects related to the Gibbs phenomenon. SUFILTER attempts to circumvent this problem by implementing a sine-squared taper intended to smooth the spectrum near corner frequencies. Even though smoothing produces a more continuous function, the transition slopes are not sufficiently moderate (especially for higher frequency bands) to completely eliminate the Gibbs phenomenon. As a result, rippling in the amplitude spectrum generates undesired noise in the narrow-band volumes.

A time-windowing procedure is applied to test the time-dependence of the 6 Hz anomalies. Figure 18 shows an inline from the post-stack volume together with its amplitude spectrum. The spectrum clearly shows relevant energy between 0 and 10 Hz, which is somewhat uncommon in traditional surface seismic data sets. Now, if we exclude the first 300 ms from the line, the windowed spectrum clearly shows that the signal, which existed between 0 and 10 Hz, has greatly diminished (Figure 19). Considering all the evidence that may disprove the geology or fracture-related validity of these low-frequency features, this thesis shifts to more robust fracture detection methods.

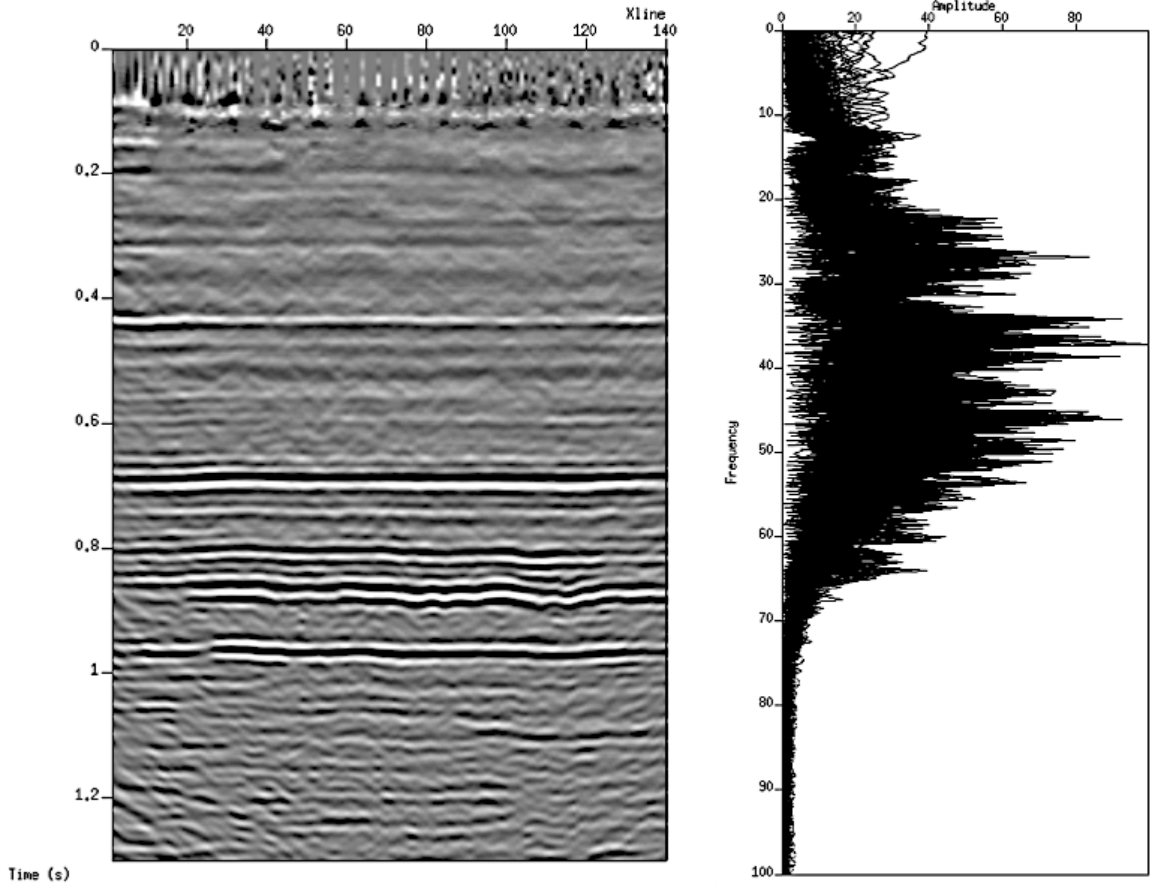


Figure 18: Arbitrary inline (left) from the Dickman post-stack and corresponding amplitude spectrum (right). Notice the relevant energy at low frequencies indicated by the spectrum. Also, notice the noise spikes at early arrival times (< 200 ms).

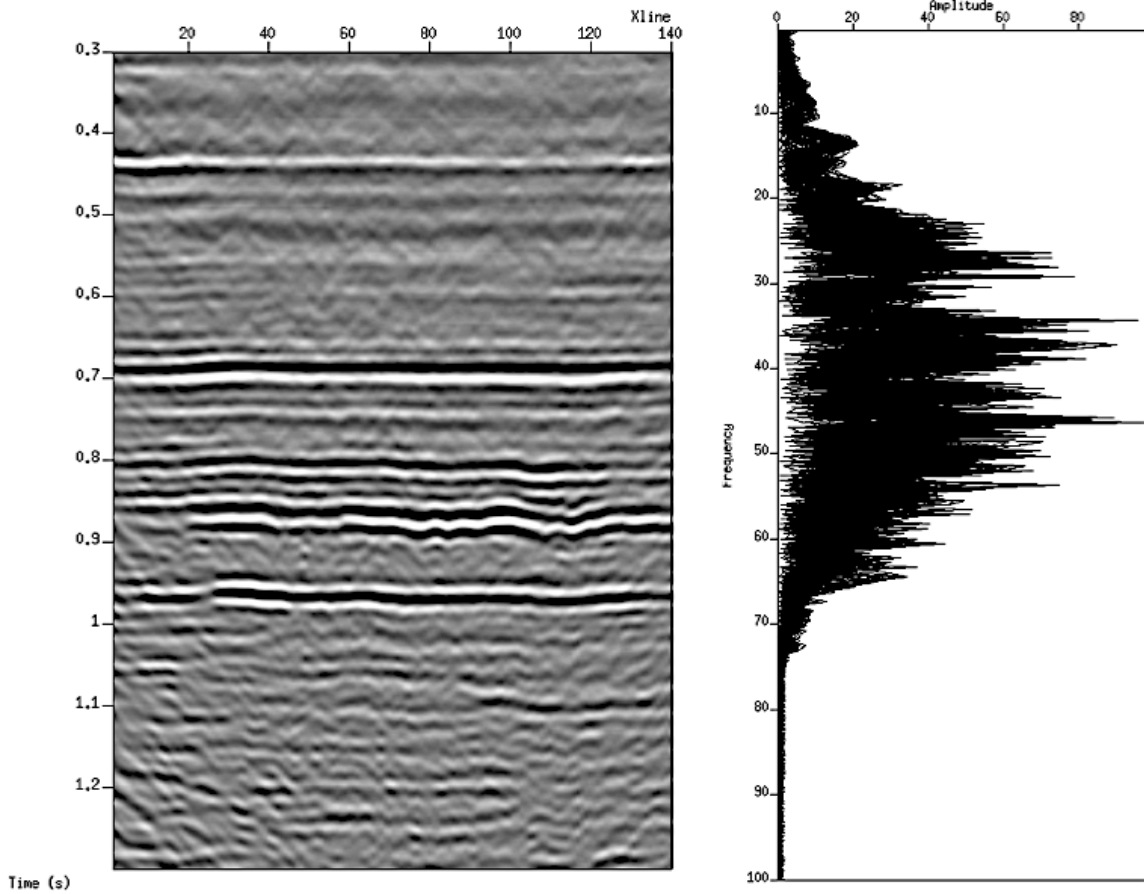


Figure 19: Same line as Figure 15, but windowed below 300 ms. Notice how the low-frequency energy is removed from the spectrum. This indicates the 6 Hz anomalies are most likely related to noise at early arrival times.

5.0 Well Log Analysis

Fracture identification from borehole methods typically rely on physical or “visual” evidence of fracturing within the borehole. The most robust data would come from image logs or core data. Image logs provide a 360 degree, un-wrapped snapshot of the borehole wall by measuring some physical property of the rock. Two examples of image logs are the formation micro-imager log (FMI), which measures formation resistivity, and the borehole televiewer (BHTV), which measures the transient time and amplitude of acoustic waves reflected from the wellbore. The major drawback of image logs is that they are expensive and proprietary in terms of availability. Core allows one to actually examine the rock from the wellbore. However, a cored section is not an in situ representation of borehole conditions. Also, core sampling may be sparse, perhaps skipping over the interval of interest all together.

If the previous data types were unavailable, then an alternative approach is to use our knowledge of conventional well logs and their response to fracturing. These responses combined with a fuzzy inference system can be used to quantify fracture intensity within the logged interval of a wellbore.

5.1 Well Log Responses

Analyzing conventional well logs in the Mississippian interval will indicate whether fracturing is ubiquitous. Conventional well logs refer to those routinely collected by industry due to their cost-efficiency. Excluding a change in lithology, or a pore fluid change, a particular log signature may express an abrupt deviation, often in the form of a spike, when encountering a fractured interval (Crain, 2012). Although not a robust method, these anomalous occurrences make fracture identification a more objective process. However, indicators from well logs are not unique to sub-vertical fracture geometry. In carbonates, the diagenetic process leads to a complex porosity and permeability configuration. Also, surficial fluid migration during the subaerial exposure of pre-Pennsylvanian rocks created a convoluted network of compartmentalized fractures lacking any preferred orientation (Nissen et al., 2009). Depending on the type of logging tool used, a log response may reflect any of these geometries. Common conventional well logs include the gamma ray, acoustic sonic, caliper, density, neutron porosity, resistivity, photoelectric index, and spontaneous potential. The following describes conventional log responses to fracturing based on the observations of Crain (2012).

The gamma ray log (GR) measures the radioactivity of a formation. Rocks that contain an abundance of radioactive elements will generate a high response on the log. Because radioactive elements are typically associated with shale, the gamma ray curve is primarily used to calculate the volume of shale in a formation. However, an increase in the gamma ray that is not accompanied with an increase in shale

volume in the formation can be a fracture indicator. Assuming a competent reading, this situation requires the fractures to be filled with a radioactive material.

The acoustic sonic log (DTp) measures the transient time of an acoustic wave through a formation. Upon interaction with a fracture, the initial wave train generated by the pulse attenuates due to the deflection of energy at the fracture interface, resulting in a severely low amplitude response. This phenomenon is known as cycle skipping and causes a rapid increase in the recorded transient time.

The caliper log (CAL) measures the borehole diameter. Sub-vertical fracturing may create an elongated borehole along the strike of the fracture. Conversely, the loss of circulation due to filtrate invasion in fractures causes a thicker mud-cake buildup resulting in a narrower borehole. However, mud-cake buildup is associated with permeable formations in general and, therefore, does not necessarily indicate the presence of fracturing.

The density log (RHOB) is a continuous measurement of formation bulk density. The density tool uses two pads: a short spaced and a long spaced detector. If both detectors read the same value then both pads are in contact with the borehole wall and no compensation or correction to the recorded density value is needed. However, disagreement between the two usually means the presence of mud-cake between the detectors and the borehole wall. In this case, a correction is recorded and applied to the long space detector value. Regarding fracture indicators, the density log sees total formation porosity and a fluid-filled fracture will reduce the bulk density of the formation. Also, an erratic density correction (RHOC) display

reflects high-frequency compensation to mud-cake that may indicate the presence of fracturing.

The neutron log also measures total formation porosity and may show a high-porosity spike similar to the density log when encountering a fractured formation. A high porosity spike from the density log unaccompanied by one from the neutron log may also indicate the presence of fracturing.

The resistivity log is a continuous measurement of formation resistivity and reflects the conductivity of the formation fluids. Resistivity tools that simultaneously measure resistivity at different formation depths are used for fracture identification. If formation resistivity is less than mud resistivity, the shallow curve (near-borehole conditions) will read higher resistivity values compared to the deep curve (formation conditions). Open fractures allow mud filtrate to penetrate deeper into the formation causing the deep and shallow resistivity curves to converge or even crossover. This crossover effect can be a useful fracture indicator; however, the porosity, permeability, effective pressure, and fluid saturation in the formation ultimately control this behavior.

The photoelectric index log (PE) measures photoelectric absorption. The tool measures the absorption of gamma rays by the formation after they have traveled such a distance in which their energy level falls below a certain threshold. This curve is used in conjunction with other logging information to determine the lithology of a formation. During the drilling process drilling mud generally invades fracture zones within a formation. When this occurs a sharp spike in the PE curve is

commonly observed. This effect is recorded by the logging tools due to the higher photoelectric index of the mud as compared to the surrounding formation. Table 1 summarizes the fracture log responses.

Well log	Response to fracture
Gamma Ray	High gamma ray spike due to clay filled fracture
Acoustic Sonic	Long travel time spike due to cycle skipping
Density	Reduction in density due to mud invasion
Density Correction	Large density correction in stiff rock due to compensation of mud invasion
Caliper	Borehole elongation/contraction due to horizontal stresses/mud-cake buildup
Shallow/Deep Induction	Resistivity curves will converge or crossover
Photoelectric Index	Anomalously high reading due to mud filled fracture

Table 1: Summary of conventional well log responses to fracturing

5.2 Fuzzy Set Theory

A classical set, or non-fuzzy set, uses a sharp boundary to distinguish adjacent sets of data. On the other hand, a fuzzy set allows transition, or overlap to occur between adjacent sets. Membership functions, which define the fuzzy sets, quantify the degree of overlap by assigning membership grades between the values of 0 and 1. Figure 20 illustrates an example described by Demicco and Klir (2004) of a classical set versus a fuzzy set. Here we see that sedimentary grain size is broken up into four general categories. The non-fuzzy set incorporates crisp boundaries of grain diameter to designate which category (non-fuzzy set) a particular grain size belongs to. That is to say a grain having a diameter of 1.999 mm would belong to the “sand” category. However, the fuzzy set would see that same grain essentially belonging equally to both the “sand” and “gravel” categories (fuzzy sets) since the transition of the membership functions is centered on 2 mm.

For a universal set X , a fuzzy set A belonging to X is defined as: $\mu_A: X \rightarrow [0,1]$, where $\mu_A(x)$ denotes the membership function for fuzzy set A evaluated at an element x of X (after Roget et al., 1997). As mentioned, the membership function assigns a value between 0 and 1 for $x \in X$. For this application, a universal set X would be the set of digitized values, x , from a well log.

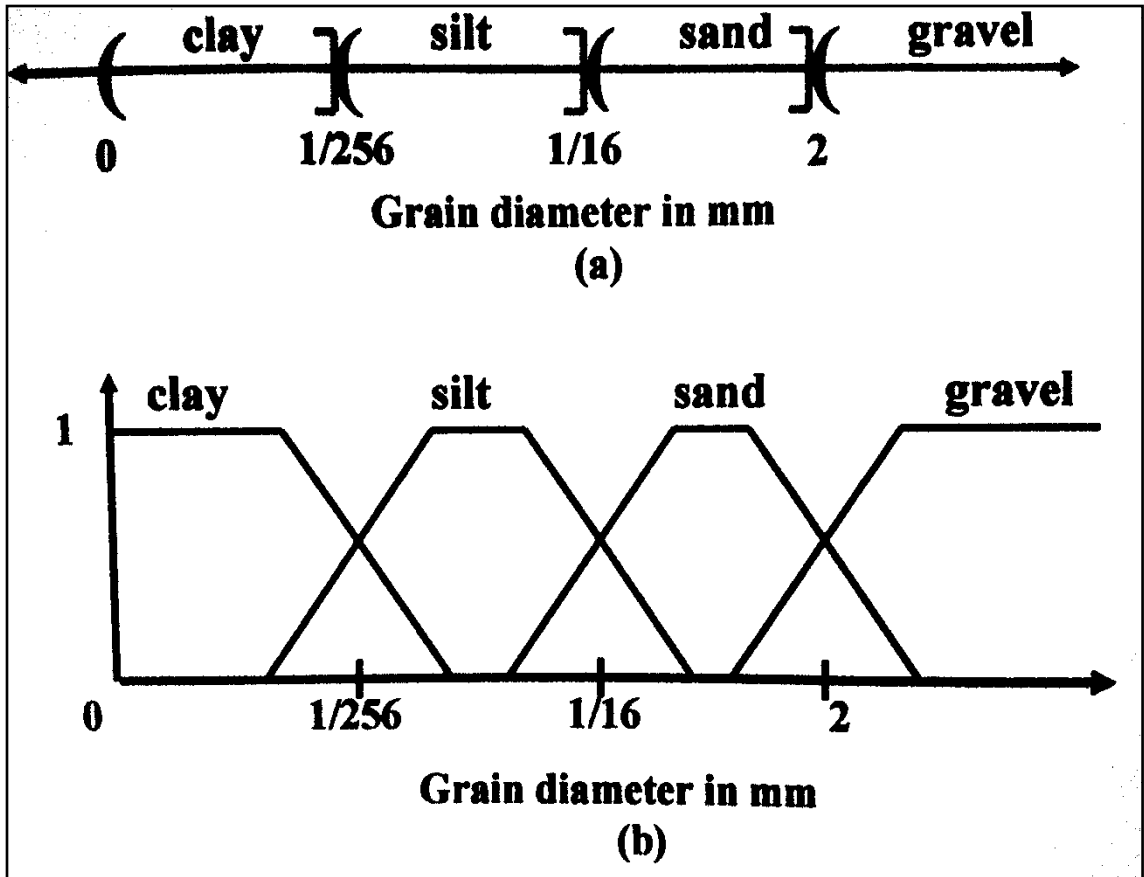


Figure 20: Comparison of grain size classification using a classical set (a) and a fuzzy set (b). A classical set incorporates crisp boundaries while a fuzzy set allows overlap to occur. Modified from Demicco and Klir (2004).

5.3 Fuzzy Inference Systems

A Fuzzy Inference System (FIS) automates our cognitive progression, regarding decision-making or drawing conclusions from an assortment of information. The system incorporates fuzzy sets and fuzzy logic to make an “inference” based on a priori knowledge of the problem (Roger et al., 1997). An FIS schematic is shown in Figure 21. The system consists of 5 steps: 1) fuzzification of the inputs, 2) application of linguistic operators, 3) implication, 4) aggregation, and 5) defuzzification (Mathworks, 2006). In the first step, parameterized membership functions categorize the input information into fuzzy sets. Steps 2 through 4 propose stipulations and organize the fuzzy sets in a manner that mimics the natural human thought process. Step 5 applies a balancing operator reducing the aggregated fuzzy sets into a single output value. The following analysis is carried out using the Fuzzy Logic MATLAB toolbox described in Appendix A.

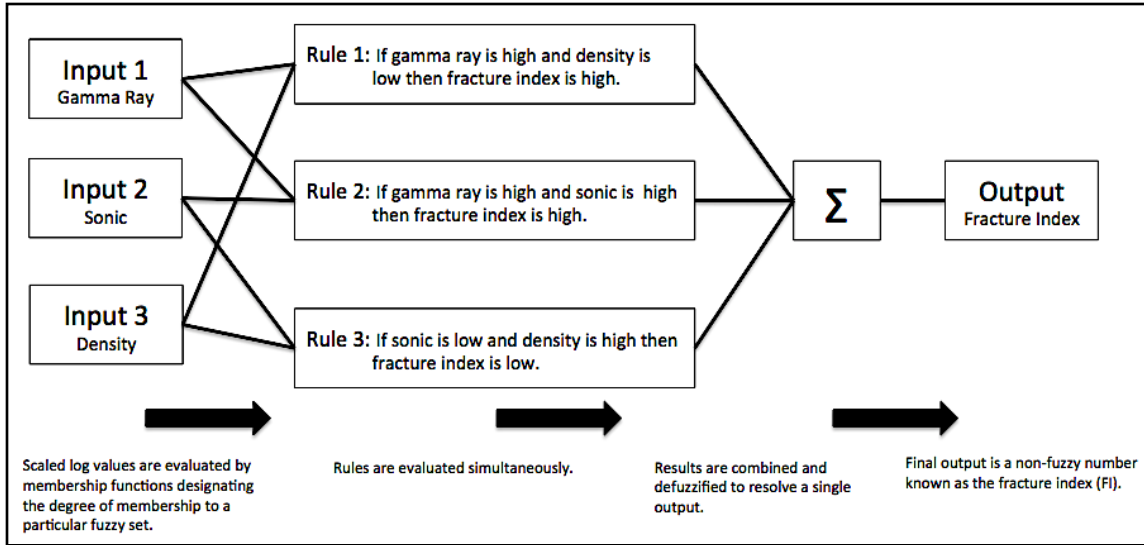


Figure 21: Schematic describing the organization of a fuzzy inference system. The process consists of the following steps: fuzzification of the input, application of the linguistic operators, the composition of the rules, and the defuzzification process, which accounts for interference in the output fuzzy set.

For this application, an FIS creates a non-linear transformation from log values (the input) to fracture index (the output). The FIS evaluates multiple log curves in parallel and outputs a value estimating the likelihood of fracturing for a given depth. The fracture index (FI) is not an inherent property of a particular rock unit, rather a relative scale of fracture intensity. From our knowledge of conventional well logs and their response to fracturing, we can intelligently devise an FIS that will filter out background information and yield only desired fracture indicators.

A similar method to that of Martinez et al. (2001) is adopted here to identify fracturing from conventional well logs. First, the log data is preconditioned prior to input. A 6-point running average filter is applied to the data designating a background value to be compared with the recorded log value. Then, the filter

average at a log sample is subtracted from the log value at that particular sample; this will be known as the deviation value. Since spikes in the log curve usually represent fracturing in the borehole, this step enhances that portion of the signal resulting in a quantified characteristic of the log curve that is not value specific. The only exception is that this filter is not applied to the shallow/deep resistivity ratio. Fracturing causes these curves to converge or crossover, meaning that the shallow will have a lower resistivity reading than the deep. The shallow/deep resistivity ratio itself is a fracture indicator and, therefore, does not require any filtering.

Next, a scaling function is applied to the deviation values:

$$Z_i = \frac{x_i - a}{b - a}, \quad (1)$$

where x_i is the deviation value at log sample i , a and b are the global minimum and maximum deviation values respectively (global meaning from the entire curve), and Z_i is the scaled deviation value for log sample i . The scaled deviation values will now range between 0 and 1. This process accounts for the discrepancy in measured values due to multiple log curves. For example, the resistivity log values typically range one or two orders of magnitude greater than the density log. If scaling were not applied, membership functions would be log and value dependent and the process of defining them would become a tedious task.

It might seem practical to take the absolute value of the deviations before applying the scaling function. Strong deflections, positive or negative, will scale to values approaching 1 while stable data will scale to values approaching 0. However, this step is avoided in order to preserve the polarity of the deflections in the data.

Therefore, strong negative deviations will map to values that approach 0 while strong positive deviations will map to values approaching 1. Stable data will approach values near 0.5.

After preconditioning the log vales, fuzzy sets are established via membership functions. A membership function uses a linear or non-linear curve to assign a grade that falls between 0 and 1 to an input value, designating the degree of membership to a particular fuzzy set. Choosing the class of membership function depends on how well the user understands the organization of the input (Roger et al, 1997). For this application, the preconditioning step categorizes any potential fracture indicators from the log information into a specific range of values (scaled deviation values), which can be readily deciphered by the membership functions parameterized over that range. However, for problems that are not intuitive, optimization techniques are often applied (Roger et al., 1997).

Sigmoidal membership functions are used for fracture indicators that correlate with strong positive or negative deviations in the data. The curve is parameterized by the following equation:

$$sig(x; a, c) = \frac{1}{1+e^{-a(x-c)}}, \quad (2)$$

where a defines the slope at the crossover point $x=c$. The crossover point is where the value of the function equals 0.5. The sign of a determines in which direction the curve converges to one. Figure 22 describes the sigmoidal membership functions.

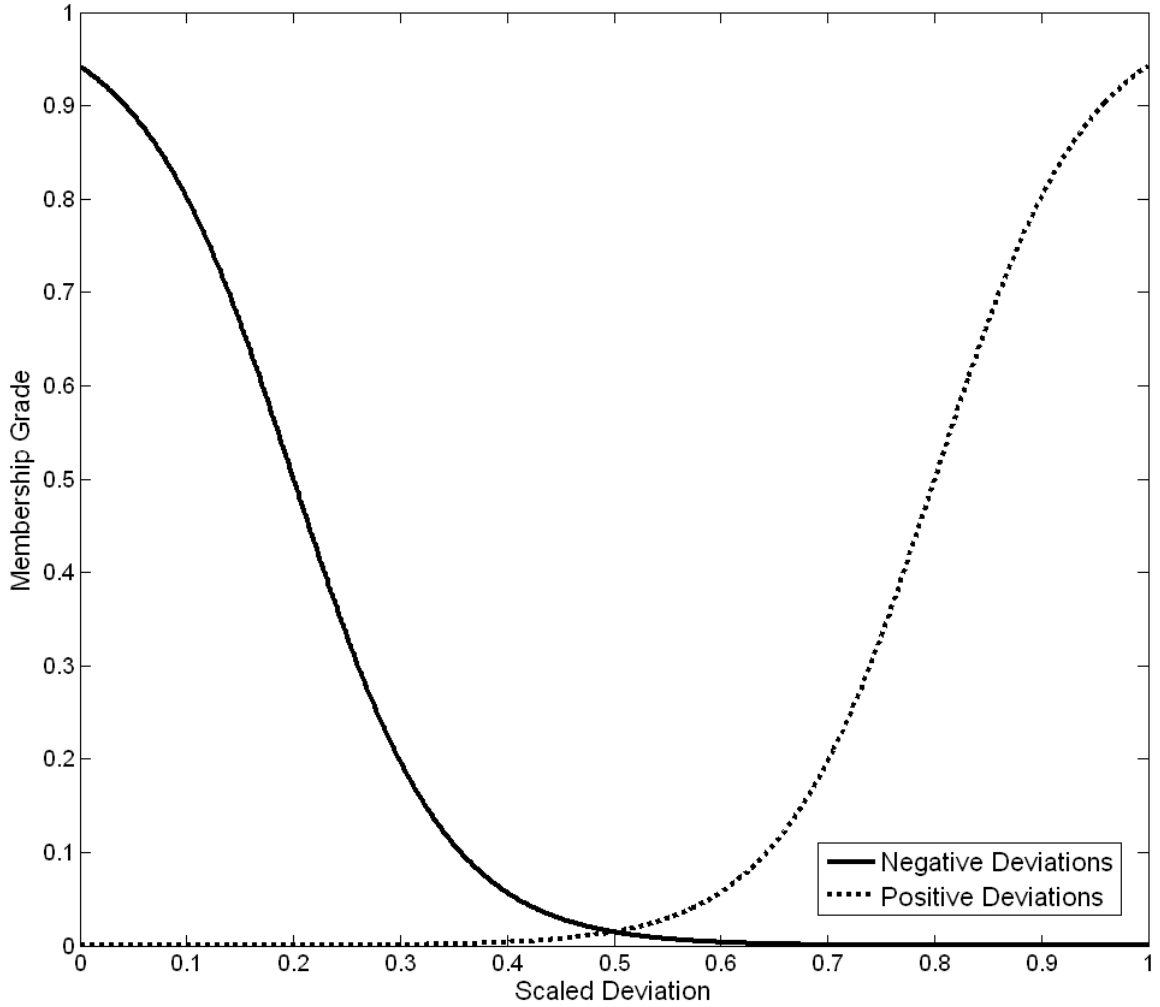


Figure 22: Plot of sigmoidal membership functions used in the analysis. Scaled deviation from background is plotted on the horizontal axis; membership grade is plotted on the vertical axis. The solid curve is designed for strong negative deviations. The dashed curve is designed for strong positive deviations.

An inverted bell curve is used for fracture indicators associated with both positive and negative deviations in the data. This membership function is limited to the caliper since fractures can cause borehole elongation or borehole contraction. The following equation parameterizes the inverted bell curve:

$$bell(x; a, b, c) = \frac{1}{1 + \left| \frac{x-c}{a} \right|^{2b}}, \quad (3)$$

where a controls the width, b controls the roundness of the curve and gradient of the slopes, and c is the center point of the function. Since fracture indicators potentially live near values of 0 and 1, a negative value for b is used to invert the bell curve (Figure 23).

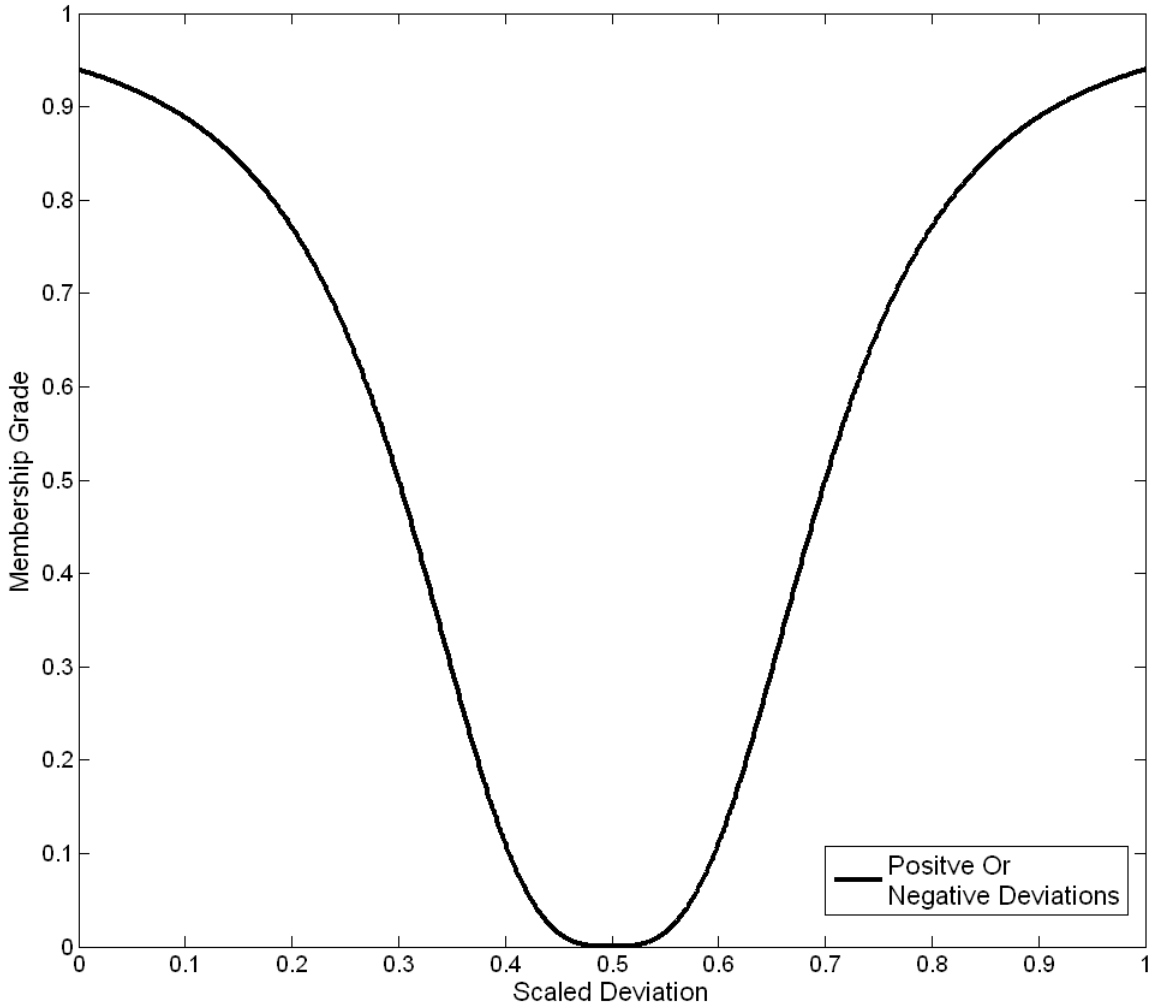


Figure 23: Inverted bell-shape membership function used in this analysis. . Scaled deviation from background is plotted on the horizontal axis; membership grade is plotted on the vertical axis. The curve is designed for fracture indicators associated with both positive and negative kicks in the data. This curve is reserved for the caliper log.

Output membership functions are also assigned. The membership grade from a collection of inputs is transposed to an output function. Two functions are defined: one corresponding to a high fracture index (**FRACTURE**) and the other to a low fracture index or (**NON-FRACTURE**). The previously described sigmoidal-type curve is used for the set of output functions. Figure 24 describes the output membership functions used in this analysis.

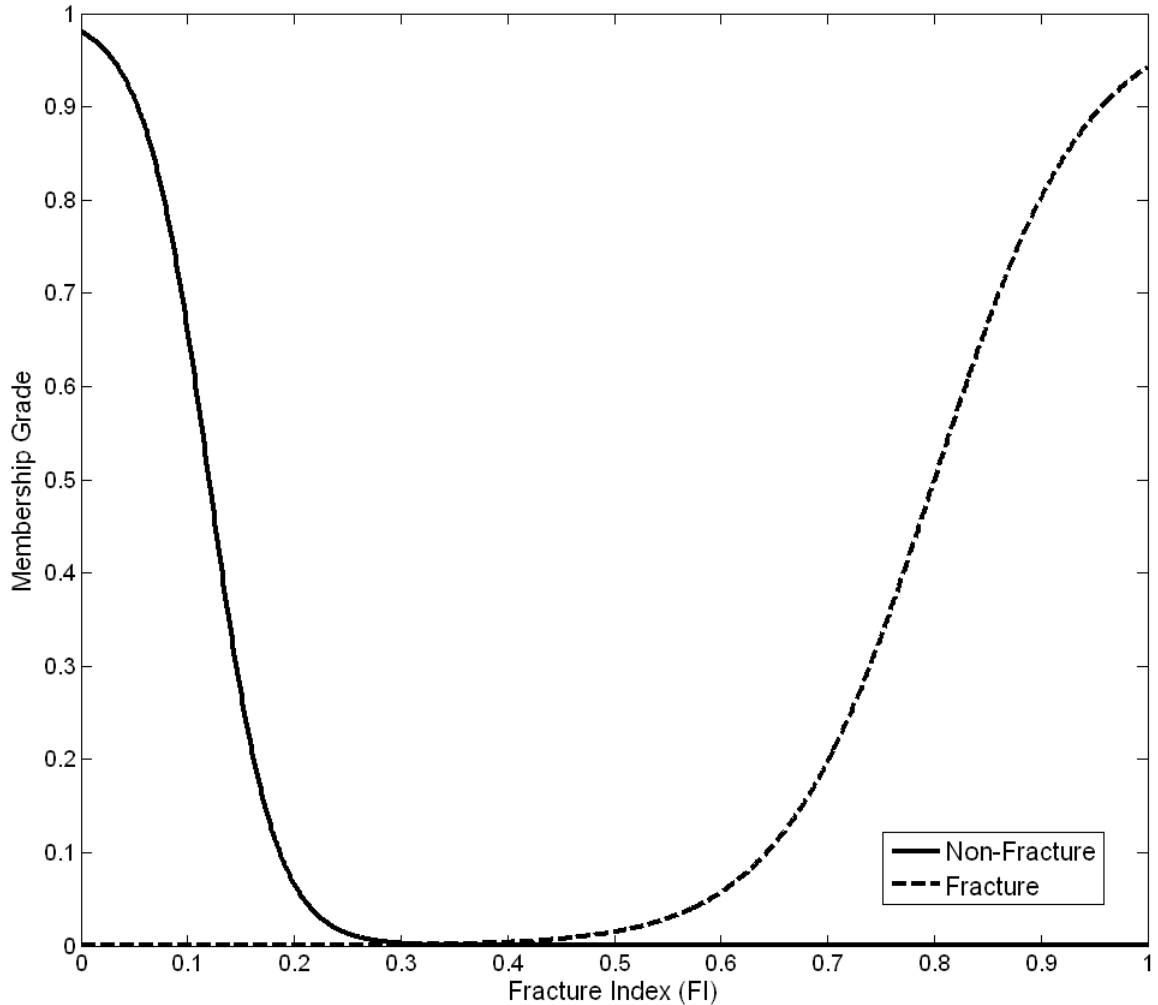


Figure 24: Plot of sigmoidal membership functions used for the output fuzzy set. Fracture index is plotted on the horizontal axis; membership grade is plotted on the vertical axis. The solid curve is designed for membership grades that do not indicate a fracture response. The dashed curve is designed for membership grades that indicate a fracture response.

Next, fuzzy operators govern how the fracture index will be specified. These operators are logical statements that structure a particular combination of fuzzy sets. Two terms will be used to classify an input fuzzy set: 1) **HIGH** and 2) **LOW**. The term **HIGH** classifies a fracture indicator with a high-scaled deviation value while the term **LOW** classifies a fracture indicator with a low-scaled deviation value (Note a low-scaled deviation value corresponds to a strong negative deviation value).

Moreover, two terms are used to classify the output fuzzy sets: 1) **FRACTURE** and 2) **NON-FRACTURE**. The term **FRACTURE** classifies a combination of input fuzzy sets indicative of fracturing (high FI) while the term **NON-FRACTURE** classifies the opposite (low FI). As mentioned, each membership function is parameterized to find values from each well log that signify fracturing. Therefore, rules are empirically formulated to determine at which depths specific combinations of well logs have high degrees of membership to their designated function. For example, the following rules search for fracture indicators:

- **If (density) is LOW and (sonic) is HIGH then (FI) is FRACTURE.**
- **If (gamma ray) is HIGH and (PE) is LOW then (FI) is FRACTURE.**

Deciding on a mixture of inputs and rules directly depend on the fracture response in a given rock type. Instead of incorporating multiple combinations of rules to dictate high fracture indices, a single combination is used, utilizing all the input logs simultaneously. This means that each input must have a relatively high membership grade to yield a significant FI value, which reduces the chance of false positives in the output. Therefore, two rules are formulated (Figure 25). The first combines all the preconditioned well logs, stipulating that each one must have evidence of fracturing to yield a high membership to the **FRACTURE** set; this will be known as the fracture indicator rule. The second essentially does the opposite; this will be known as the non-fracture indicator rule. If the input variables do not meet the criteria set by the fracture indicator rule, then the non fracture-indicator output function registers a high membership grade to the **NON-FRACTURE** set.

Applying the implication is the next step. Once all the variables for a given rule are evaluated, the output membership function needs to weigh the individual contributions of those inputs. The implication truncates the output membership function at a value that has statistical significance to the assortment of input fuzzy sets. To make sure fracture indicators are present for every well log, the selected implication operator truncates the output membership function at the value attributed to the lowest membership grade among the inputs (Figure 25).

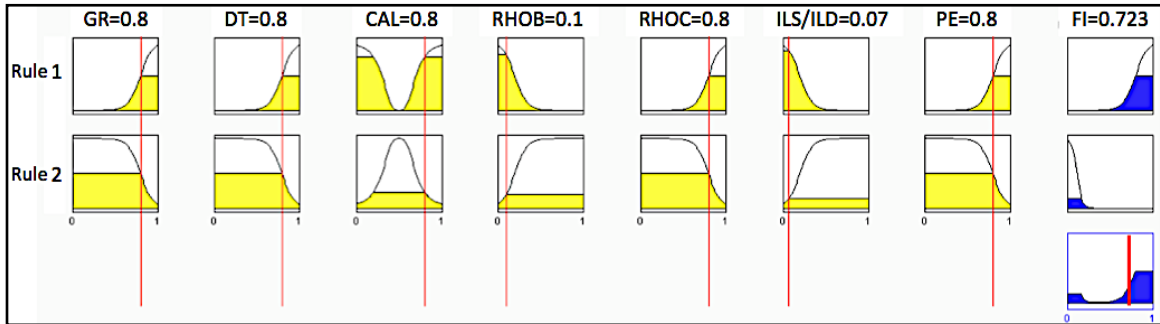


Figure 25: Snapshot representation from the Fuzzy Logic Toolbox (MATLAB, 2006) illustrating all the components of an FIS. The figure shows (1) the type of membership function assigned to each log type, (2) the assigned rules, (3) the implication, (4) aggregation, and (5) defuzzification. The fracture rule (rule 1) reads: If gamma ray is **HIGH** and sonic is **HIGH** and caliper is **HIGH** and density is **LOW** and density correction is **HIGH** and shallow/deep induction is **LOW** and photoelectric index is **HIGH** then the fracture index is **FRACTURE**. The non-fracture rule (rule 2) reads: If gamma ray is **NOT HIGH** and sonic is **NOT HIGH** and caliper is **NOT HIGH** and density is **NOT LOW** and density correction is **NOT HIGH** and shallow/deep induction is **NOT LOW** and photoelectric index is **NOT HIGH** then the fracture index is **NON-FRACTURE**. It is obvious why rule 2 is necessary. Due to the implication, if an input value did not fall under the input curve, then the defuzzification process would produce an FI value of 0.5, the function's center of mass. Since the input values used in this example are strong fracture indicators, the output registers a high FI value (0.723).

Following the implication process, there are two output fuzzy sets that correspond to the aforementioned rules (labeled 1 and 2 in Figure 25). These two fuzzy sets are then aggregated to form one output fuzzy set. Since two truncated functions are summed in this process, the aggregated fuzzy set encompasses a range of values that must be “defuzzified”. The defuzzification process extracts a single value, characteristic of the overall fuzzy set (Roger et al., 1997). The chosen defuzzification operator is the Centroid of Area (COA) calculation expressed by the following:

$$z_{COA} = \frac{\int_Z \mu_A(z) z dz}{\int_Z \mu_A(z) dz} \quad (4)$$

where $\mu_A(z)$ is the aggregated output membership function and Z represents the range of values from the aggregated fuzzy set. Figure 25 summarizes the entire FIS procedure.

5.4 Case Study

The application of an FIS for subsurface fracture characterization requires significant amounts of borehole information. A particular borehole must have a sufficient suite of conventional well logs that implicitly respond to fracturing. Data quality must be reliable in order to reduce the probability of false positives in the results. Therefore, noisy data should be recognized and discarded prior to the implementation of this algorithm. A quick-look method is to examine the caliper curve for erratic behavior, which may indicate decoupling from the borehole wall resulting from an unstable interval in the wellbore. This will directly affect other log measurements, leading to misinterpretations of fractured intervals.

Also, it is important to have fracture data, which is: 1) independent from the results and 2) provides some degree of validation of fracturing. The ideal data would consist of high-resolution image logs, or a continuously cored section from the interval of interest. Both in this case would provide direct information describing fracture abundance and geometry in the borehole. On the other hand, if such information were available for every borehole, then this entire endeavor would be unnecessary. Therefore, assuming relatively consistent geology, this type of algorithm could be used to extrapolate local fracture information to boreholes that do not have direct fracturing data.

The Dickman Field has two boreholes with conventional well logs that are suitable for an FIS application: Humphrey 4-18 and Sidebottom 6. The proximity of these wells to the spectral anomalies (Figure 26) is not optimal. However, the goal is

to understand whether the particular interval of rock encasing the Mississippian reservoir is in fact sufficiently fractured to yield anomalies in the post stack seismic volume. Borehole methods are the only means of providing ground-truth information regarding fracture geometry and abundance in the subsurface. Therefore, it is imperative to find evidence from such methods in order to validate results from seismic fracture characterization techniques that provide qualitative visual indication, such as those previously used (Nissen et al., 2009) as well as the low-frequency features in this work.

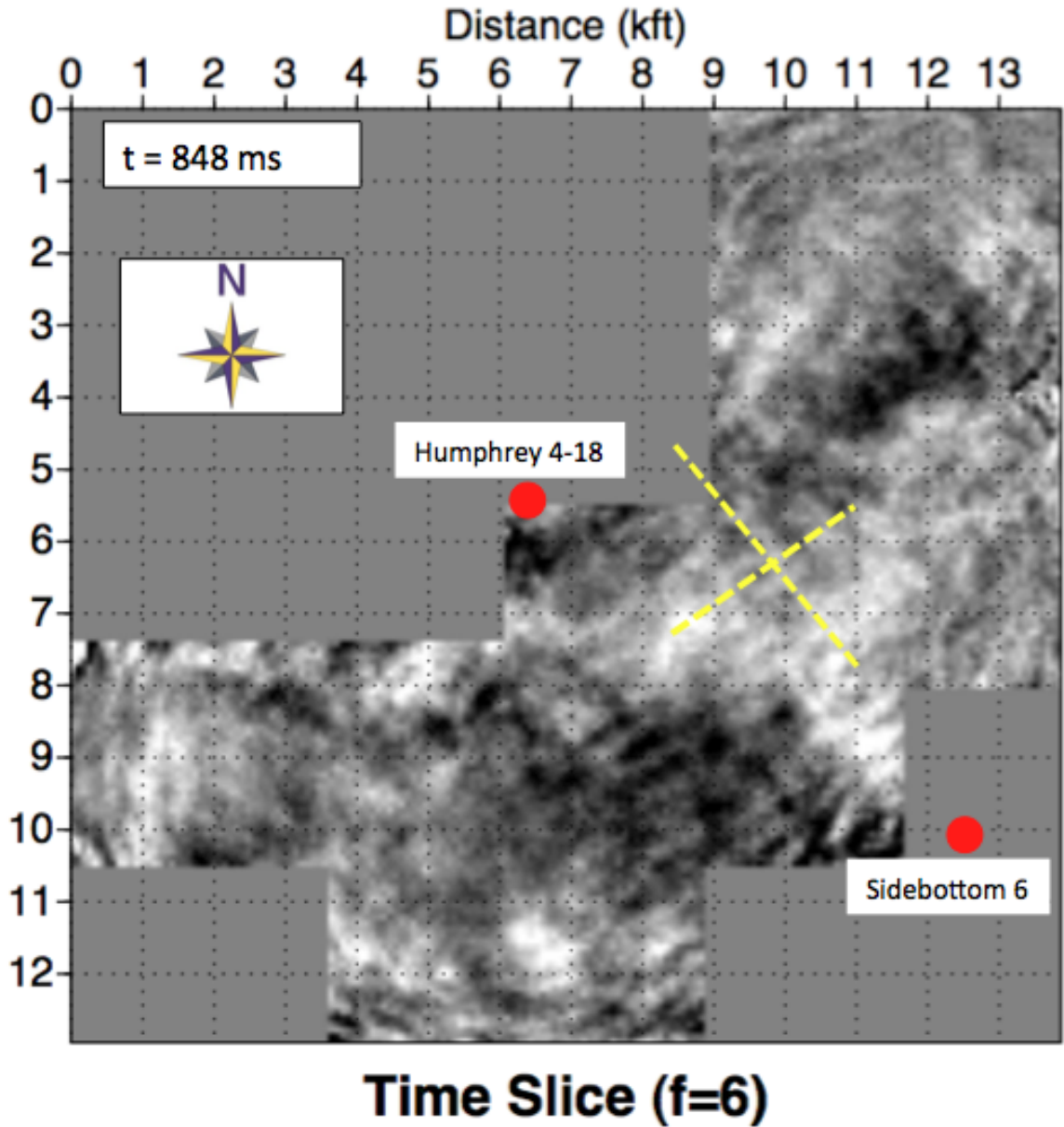


Figure 26: 6 Hz time slice showing well proximities to the 6 Hz anomalies.

The interval of interest begins approximately at the Mississippian-Pennsylvanian unconformity and extends to the base of the Osage. This interval spans -1943 to -2103 ft (-592 to -641 m) subsea in Humphrey 4-18 and -1993 to -2113 ft (-607 to -644 m) subsea in Sidebottom 6. An additional 30 ft (9 m) of

overlying Pennsylvanian section is included to test the FIS response of varying lithology (Section 7.0). Table 2 lists the well logs used in this study and Figures 27 and 28 show their curves. Both caliper logs from their respective wells show about a ± 0.4 " deviation from average, indicating a competent interval of rock encountered within the boreholes. Therefore, the data quality should be acceptable and any high-frequency deviations in the log curves are interpreted as fracturing, lithology changes, or pore fluid changes.

Log Type	Humphrey 4-18	Sidebottom 6
Caliper	Yes	Yes
P-wave Sonic	Yes	Yes
Gamma Ray	Yes	Yes
PE	Yes	Yes
Density	Yes	Yes
Density Correction	Yes	No
Deep/Shallow Induction	Yes	Yes

Table 2: Table showing list of well logs types available for this analysis.

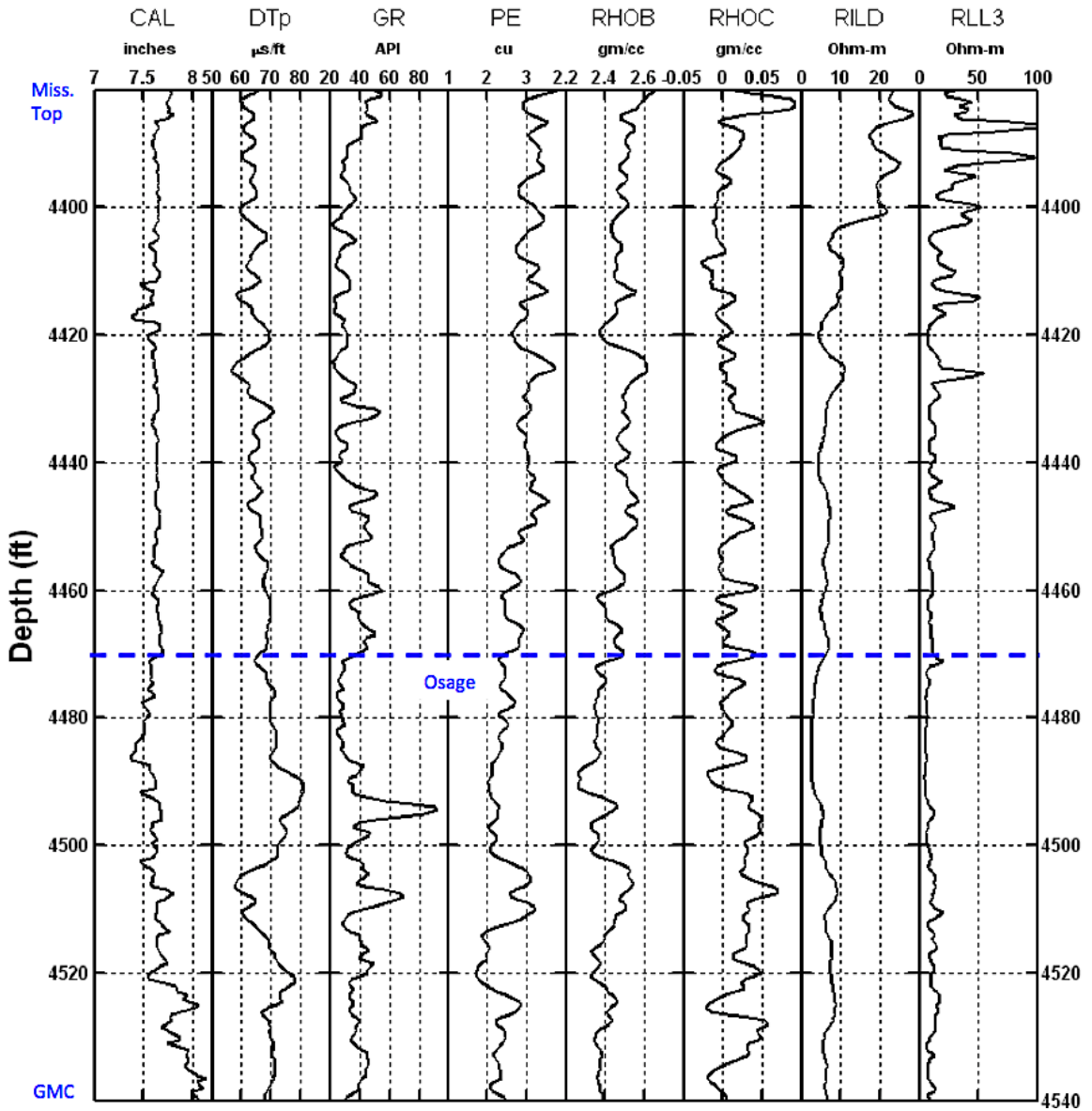


Figure 27: Plot of Humphrey 4-18 log curves used in this analysis. From left to right the log curves shown are the caliper (CAL), P-wave sonic (DTp), gamma ray (GR), photoelectric index (PE), density (RHOB), density correction (RHOC), deep induction (RILD), and shallow induction (RLL3). The depth interval spans from 4380 to 4540 ft (1335 to 1384 m) MD, which covers the top of the Mississippian through the Gilmore City top (GMC). The Osage Formation top is marked.

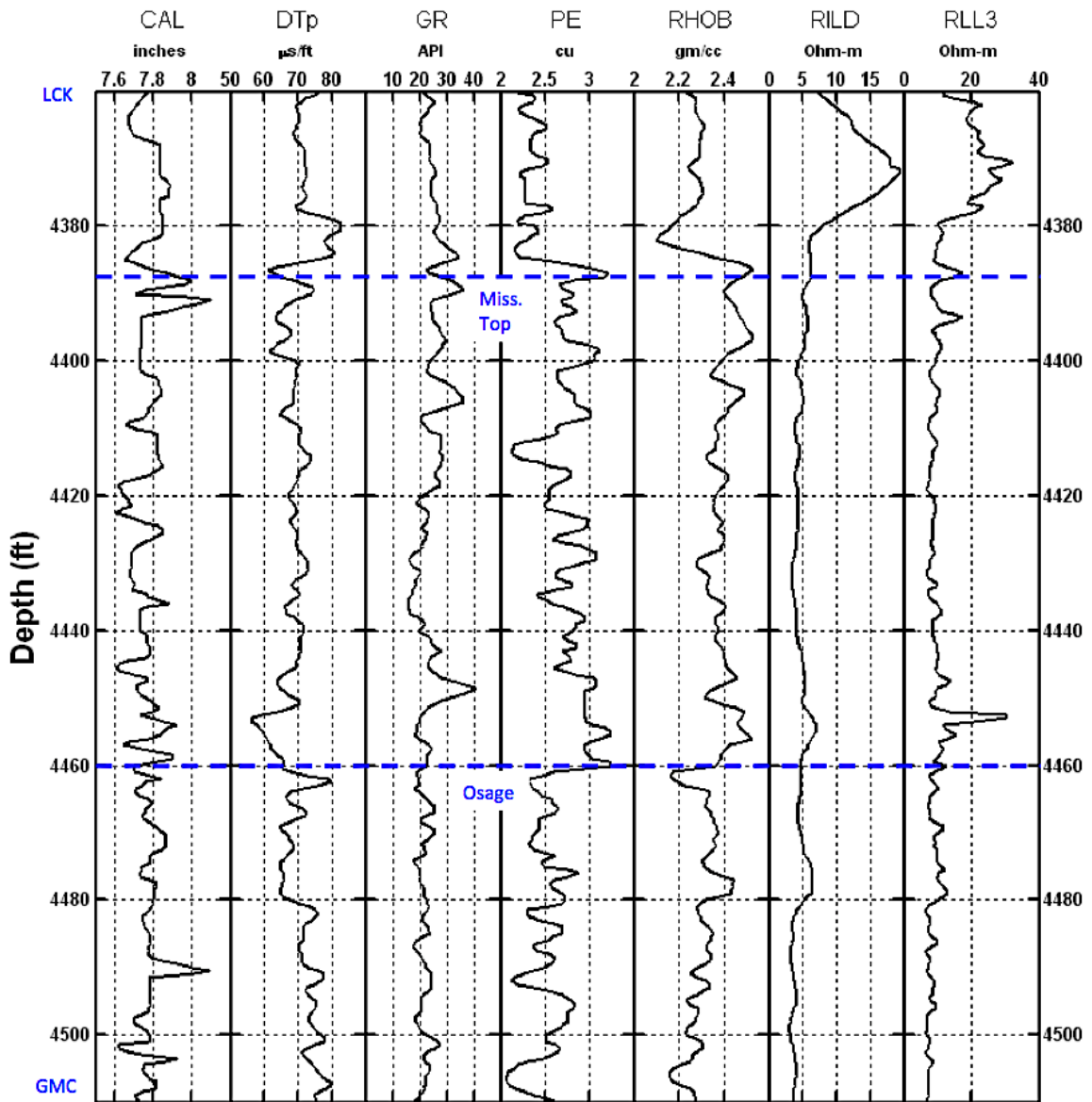


Figure 28: Plot of Sidebottom 6 log curves used in this analysis. The available log curves available for use are the same as the former with exception to the density correction log (RHOC). The depth interval spans from 4360 to 4510 ft (1328 to 1375 m) MD, which covers basal Lower Cherokee (LCK) through the Gilmore City top (GMC). The Mississippian and Osage Formation tops are marked.

Figures 29 and 30 show the FIS results for Humphrey 4-18 and Sidebottom 6 respectively. The individual log responses in the sections do not exhibit high amplitude spiking indicative of fracturing. It is obvious from the FIS scale, which

ranges from 0 to 1, that fracture intensity (FI) values are low. This is expected because a maximum of 7 stipulations are proposed (6 stipulations for Sidebottom 6); therefore, high values of FI are only achieved when the proposed rule is met in its entirety. However, when compared to the background, the FIS results do show high-amplitude spikes throughout the section. The most pronounced for Humphrey 4-18 occur at 4460 ft (1360 m) MD and 4500 ft (1372 m) MD. For Sidebottom 6, high FI values occur at 4390 ft (1388 m) MD and in the interval between 4445 and 4490 ft (1355 and 1367 m) MD. While the FIS results may provide evidence of fracturing, they do not, however, describe the geometry or whether the fractures are natural or drilling induced. Therefore, the results should be validated by direct fracturing evidence.

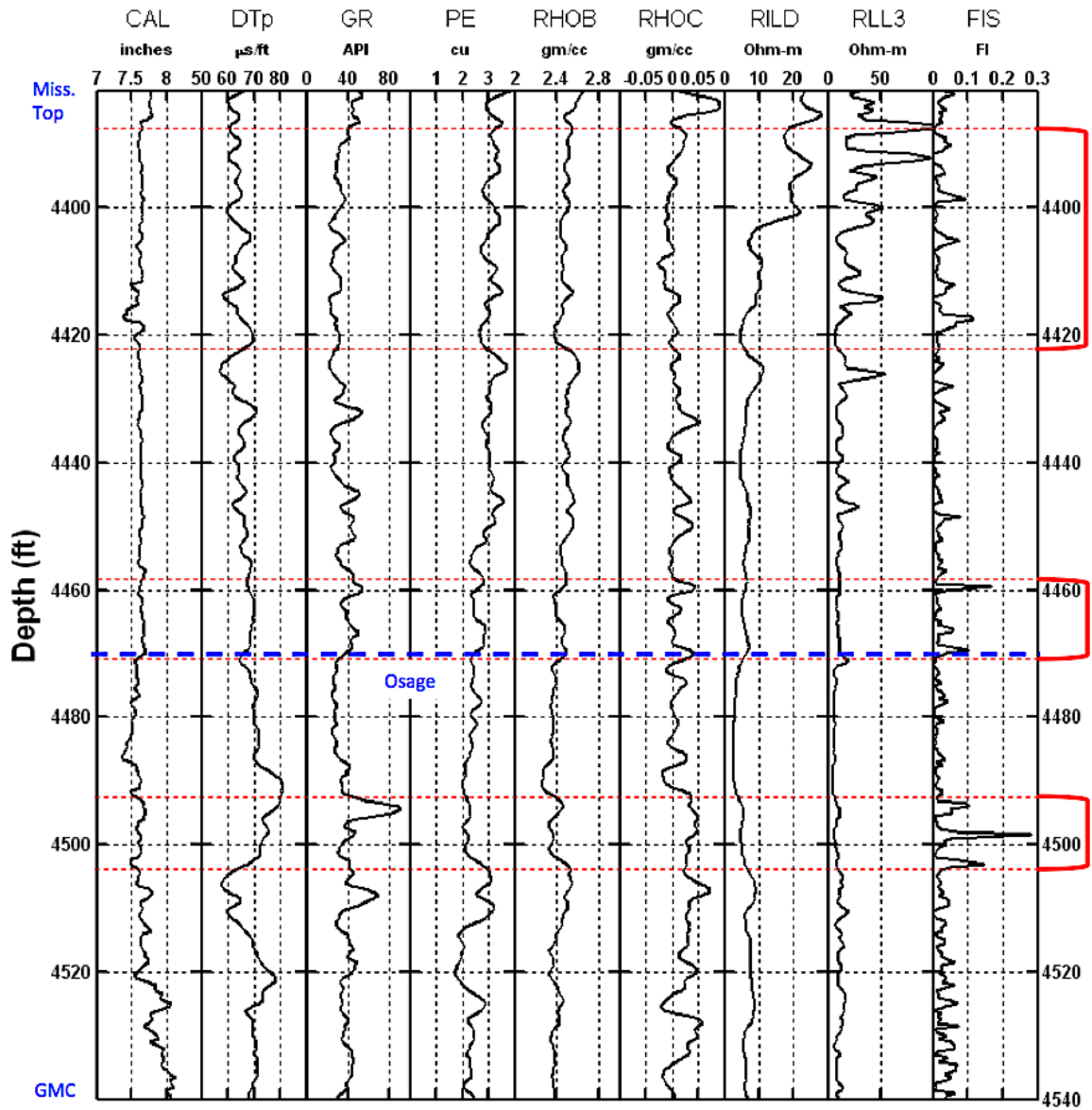


Figure 29: Humphrey 4-18 FIS results (right-most column) plotted against the input curves. The FI spikes are potential fracture indicators. The zones of interest are marked on the figure.

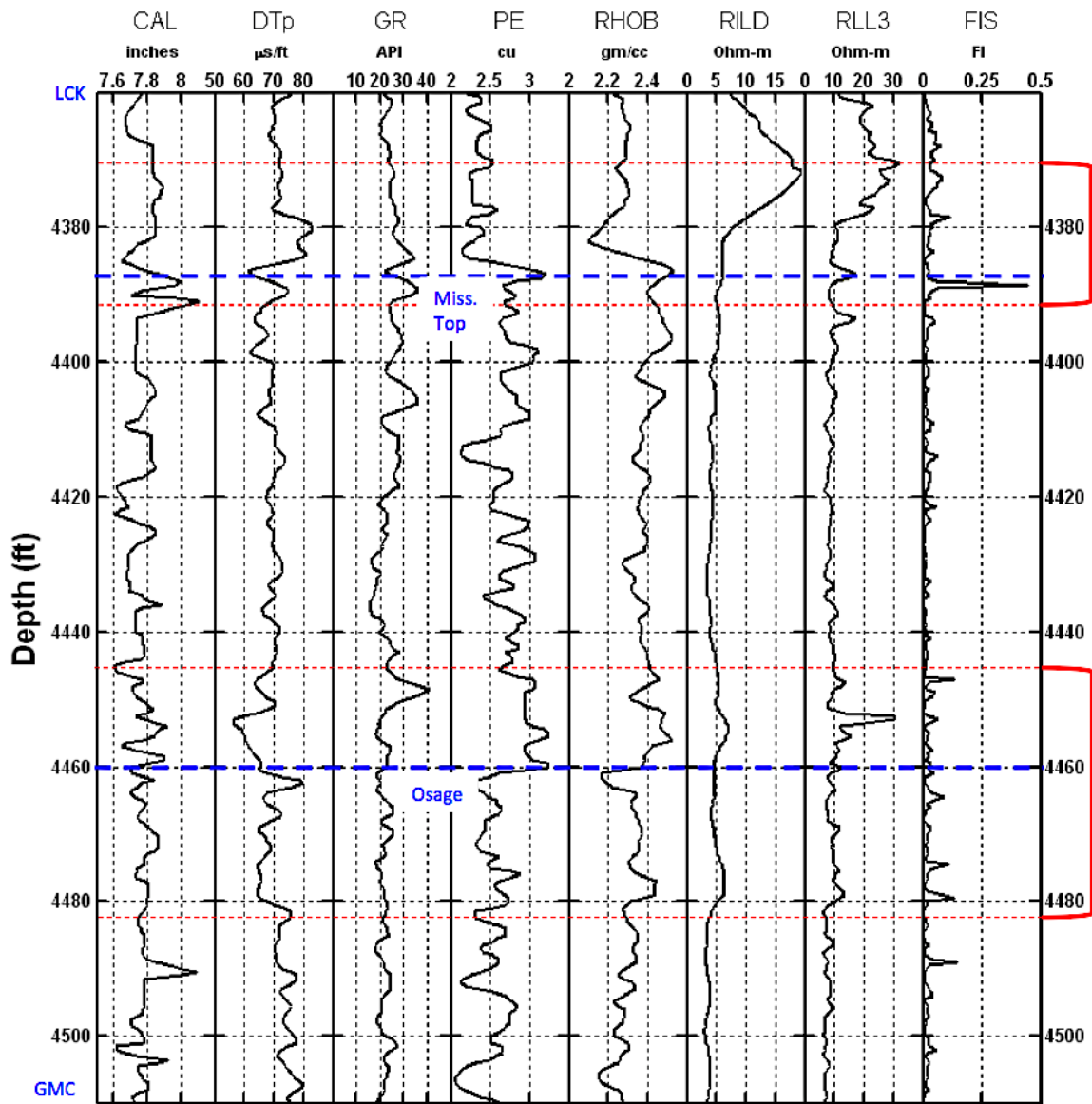


Figure 30: Sidebottom 6 FIS results (right-most column) plotted against the input curves. The FI spikes are potential fracture indicators. The zones of interest are marked on the figure.

Unfortunately, image logs and core are inaccessible for Dickman wells. Therefore, lithology strip logs are used to validate the FIS results. A lithology strip log is a subjective interpretation of well cuttings from an onsite interpreter. The log is usually composed of rock descriptions, sometimes discussing the grain size,

mineralogy, and porosity type. Consequently, misinterpretations and inaccurate descriptions of the actual rock mass are liable to exist and are most likely not rectifiable. On the other hand, the strip log can be used to rule out anomalously high FI values that correlate to lithological changes on the strip log. Barring some external effect, these high FI values can be interpreted as potential fracture indicators.

Figure 31 shows the FIS results for Humphrey 4-18 depth correlated with a lithology strip log from that well. Beginning from zone 1 (4380 to 4420 ft (1335 to 1347 m) MD), the strip log describes the rock as dolomite with vuggy and fractured porosity. The FIS is possibly responding to mud filtrate invasion due to the fractured porosity.

The rock section in zone 2 (4445 to 4475 ft (1355 to 1364 m) MD) consists of porous dolomite and chert. Specifically, the rock at the highest FI value (4460 ft (1360 m) MD) is described as brittle dolomite containing dead oil stains and chert inclusions. The FIS at this depth could be responding to fracturing, oil stains, or perhaps a chert streak. Moreover, the FI spike below this marker (4470 ft (1362 m) MD) could be responding to a fracture since it does not exactly correlate with the lithology change at 4465 ft (1361 m) MD.

The rock section in the zone 3 (4490 to 4510 ft (1367 to 1375 m) MD) consists of porous, dense dolomite with fossil casts. The strongest FI value (0.3) of the entire section occurs in this interval at 4495 ft (1370 m) MD. Considering there

are no obvious lithological influences, this high FI value could be evidence of a fracturing.

The strip log from Sidebottom 6 is missing samples throughout the majority of the analyzed Mississippian section; therefore, the FIS results cannot be constrained. On the other hand, the major FI peak (0.45), which occurs around 4390 ft (1388 m) MD, represents early Pennsylvanian channel deposits. This large peak likely represents rapid lithology changes from this depositional period.

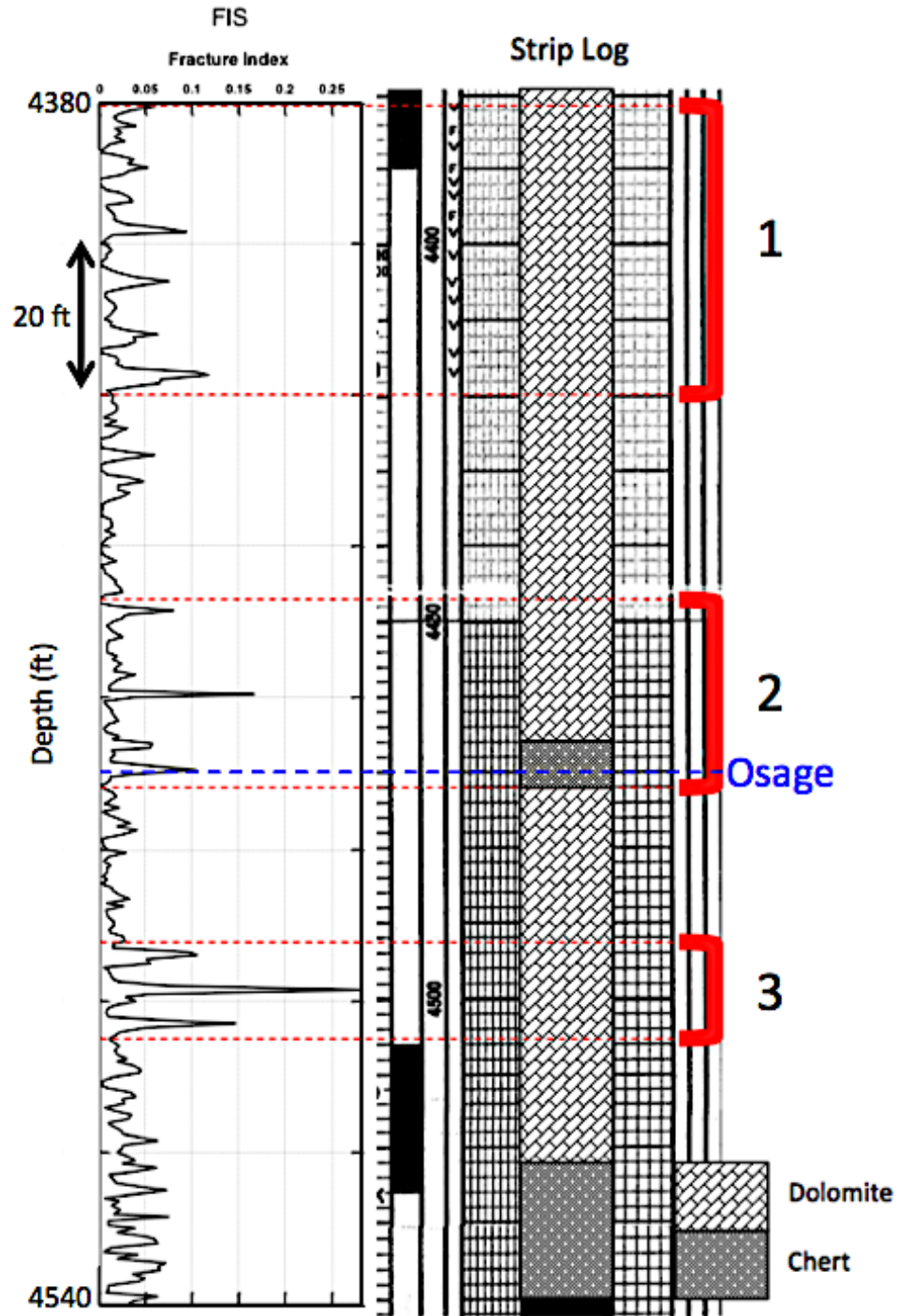


Figure 31: Humphrey 4-18 FIS results depth correlated to a lithology strip log. The log is used to rule out anomalously high FI values that correlate to lithological changes on the strip log. Anomalous zones are highlighted and labeled (1-3) in the figure.

6.0 Prestack Analysis

Natural fracture systems behave as conduits enabling the migration of fluids within, or potentially away from a reservoir. Understanding the geomechanics that govern these reservoir properties (i.e. porosity and permeability) is necessary towards constructing a proper reservoir model. Fracture information is typically obtained from borehole methods such as image logs or core analysis; also, from seismic attributes like coherence and curvature. However, borehole methods often suffer from poor spatial resolution while seismic attributes, which map the spatial distribution of faulting, may not provide a robust indication of sub-resolution fracturing, or provide information concerning principal stress orientations. Therefore, fracture characterization, on a reservoir scale, largely depends on seismic inversion methods from 3D wide-azimuth data. Methods such as Velocity Variation with Azimuth (VVAZ) and Amplitude Variation with Angle and Azimuth (AVAZ) are routinely used toward detecting sub-seismic resolution fracturing or stress fields. VVAZ is less influenced by processing, but suffers from poor vertical resolution and is, therefore, limited to detecting anisotropic effects from the overburden. Conversely, AVAZ is strongly influenced by processing, but conveys anisotropic information from the reflecting interface. Although AVAZ potentially improves resolution, both methods are routinely conducted in parallel for an unbiased comparison. The following will discuss P-wave AVAZ theory and applications.

6.1 HTI Model

Parallel fractures with spacing significantly less than seismic wavelength create directional variations in reflectivity and traveltime. In other words, vertically aligned fractures produce azimuthal anisotropy. The simplest case is a transversely isotropic medium with a horizontal axis of symmetry (HTI). An HTI medium describes vertical, penny-shaped cracks embedded into an isotropic background, and sometimes is a sufficient approximation for isotropic rock masses with unidirectional, sub-vertical fracture sets (Thomsen, 1995). In more realistic cases, there are often conjugate sets, and if orthogonal, the model extends to orthorhombic symmetry. Also, transverse isotropy with a vertical axis of symmetry (VTI) coupled with a vertical fracture set describes an orthorhombic symmetry (Tsvankin, 1997). In regards to AVAZ, multiple fracture sets may significantly reduce detectable anisotropy in P-wave datasets (Chen et al., 2005). Orthorhombic symmetries are not discussed in detail in this work.

The coordinate system of the HTI model is defined with respect to the fracture normal (x_1), strike (x_2), and vertical axis (x_3) (Figure 32). For consistency, Rüger (1998) denotes the (x_1, x_3) plane as the symmetry axis plane and the (x_2, x_3) plane as the isotropy plane. With exception to the orthogonally polarized shear modes, waves propagating in the isotropy plane do not exhibit any velocity variations.

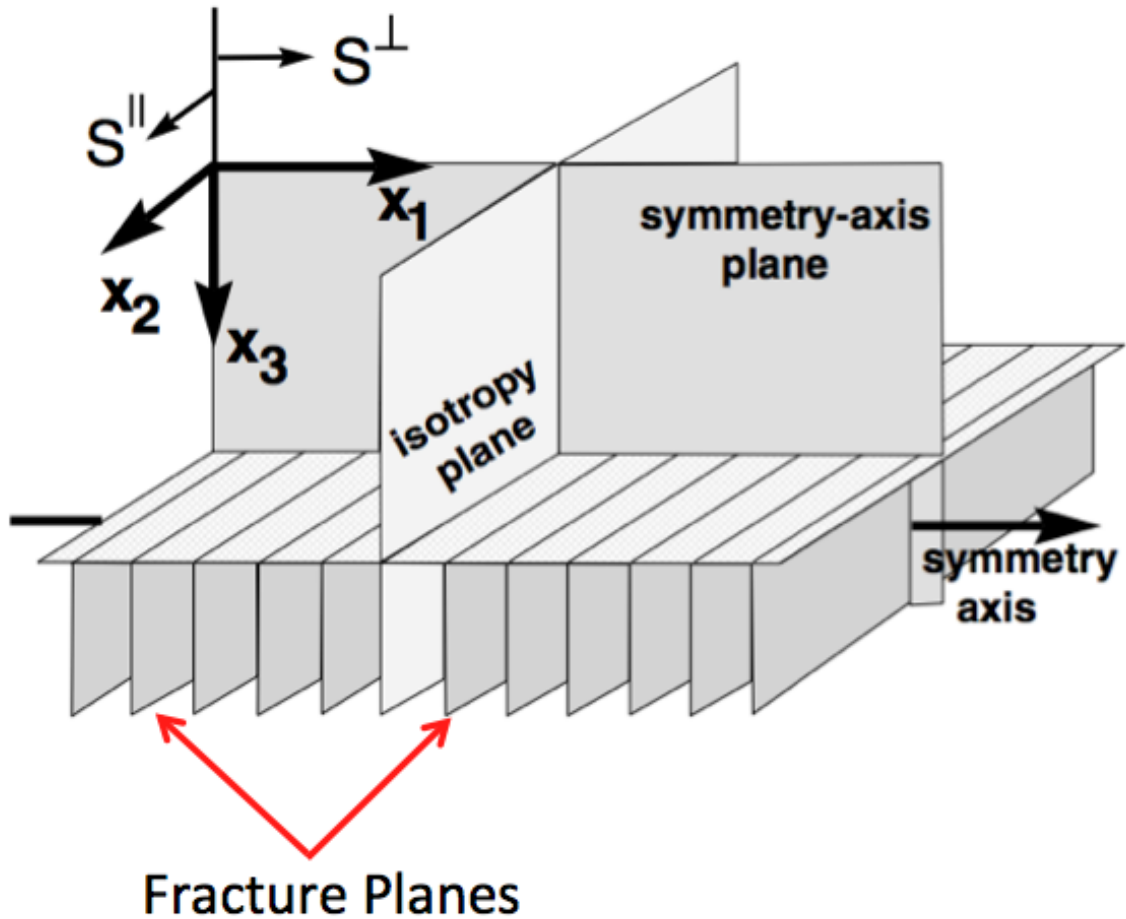


Figure 32: HTI model with axis notation. The isotropy plane corresponds to the fracture plane. P-waves traveling in the isotropy plane travel faster than those in the symmetry-axis plane. S^{\parallel} and S^{\perp} describe the polarization direction of shear modes relative to the isotropy plane. Shear waves polarized in the isotropy plane travel faster than those polarized in the symmetry-axis plane. Modified from Rüger (2002).

For HTI symmetry, the elastic stiffness tensor C_{ij} , and density ρ , Rüger (1998) modifies the original Thomsen parameters (Thomsen, 1986) with respect to the HTI vertical axis (Table 3). The superscript (V) makes reference to the vertical axis (x_3); α is the p-wave velocity in the isotropy plane, and β defines the velocity for shear modes in the isotropy plane. These anisotropy parameters provide an analog to their VTI equivalents regarding wave propagation in the symmetry plane (Rüger,

1998). Consequently, $\delta^{(V)}$ governs the deviation from isotropy for near-vertical wave propagation, while $\epsilon^{(V)}$ describes the difference between vertical and horizontal p-wave velocities. Since α is the reference velocity for the HTI model and, moreover, the velocity for vertical propagation is usually greater than for horizontal propagation, $\delta^{(V)}$ and $\epsilon^{(V)}$ are negative values. A thorough account of the HTI coefficients can be found in Rüger (1998, 2002).

	c_{ij} – notation	generic Thomsen notation	weak anisotropy
α	$\sqrt{c_{33}/\rho}$	$V_{P0} \sqrt{1 + 2\epsilon}$	$V_{P0} (1 + \epsilon)$
β	$\sqrt{c_{44}/\rho}$	$V_{S0} \sqrt{1 + 2\gamma}$	$V_{S0} (1 + \gamma)$
β^\perp	$\sqrt{c_{55}/\rho}$	V_{S0}	V_{S0}
$\delta^{(V)}$	$\frac{(c_{13} + c_{55})^2 - (c_{33} - c_{55})^2}{2c_{33}(c_{33} - c_{55})}$	$\frac{\delta - 2\epsilon(1 + \epsilon/f)}{(1 + 2\epsilon)(1 + 2\epsilon/f)}$	$\delta - 2\epsilon$
$\epsilon^{(V)}$	$\frac{c_{11} - c_{33}}{2c_{33}}$	$-\frac{\epsilon}{1 + 2\epsilon}$	$-\epsilon$
$\gamma^{(V)}$	$\frac{c_{66} - c_{44}}{2c_{44}}$	$-\frac{\gamma}{1 + 2\gamma}$	$-\gamma$
γ	$\frac{c_{44} - c_{66}}{2c_{66}}$	γ	γ

Table 3: Notations of the anisotropic parameters for HTI media. From Rüger (2002).

6.2 AVAZ Theory

The three-term linearization of the Zoeppritz equation for the P-P reflection amplitude as a function of incident angle (θ) between isotropic media is expressed as:

$$R_{pp}(\theta) \cong A + B\sin^2\theta + C\sin^2\theta\tan^2\theta \quad (5)$$

(After Shuey, 1985). A is the normal incidence P-wave reflection coefficient, B is the AVO gradient, and C is the curvature term, which is influenced by the contrast in P-wave velocities for angles of incidence approaching the critical angle. Connelly (1999) defines terms A , B , and C in full. Equation (1) is usually truncated after the gradient term due to poor signal-to-noise ratio commonly associated with far offsets (i.e. an offset-to-depth ratio greater than one). The AVO gradient is a function of the contrast in Poisson's ratio across the reflecting interface and can be a robust pore fluid discriminator (Hilterman, 2001). However, this three-term approximation assumes isotropic behavior and, therefore, does not account for the azimuthal component in reflectivity, which may be related to systematic type of fracturing.

Azimuthal variations in the AVO gradient can be a direct indicator of azimuthal anisotropy in the subsurface. Rüger (1998) modifies this approximation to account for azimuthal reflectivity variations in the media bounding the reflecting interface. For an HTI/HTI interface with an equivalent symmetry axis orientation above and below an interface, the P-P reflection amplitude as a function of incident angle (θ) and azimuth (ϕ) relative to the symmetry axis is given by:

$$R_{pp}(\theta, \phi) \cong A + \frac{1}{2} [B + D \cos^2(\phi)] \sin^2(\theta) + E \sin^2 \theta \tan^2 \theta, \quad (6)$$

where

$$D = \left[\Delta \delta^{(V)} + 2 \left(\frac{2\bar{\beta}}{\bar{\alpha}} \right)^2 \Delta \gamma \right],$$

$\Delta \delta^{(V)}$ and $\Delta \gamma$ refer to the changes in anisotropic parameters across the reflecting interface; $\bar{\beta}$ and $\bar{\alpha}$ refer to the average vertical velocities across the reflecting interface; A is the normal incidence P-wave reflection coefficient, B is the isotropic AVO gradient, which is azimuthally independent, D is the azimuthally dependent component of the AVO gradient, which has a $\cos^2(\phi)$ variation, and E is the anisotropic term for angles of incidence approaching the critical angle. Just as with conventional AVO, information regarding the high angle term requires wide-azimuth, far-offset data with a high signal-to-noise ratio while also having considerable fold. Although useful for estimating anisotropic parameters (Rüger, 1998), the high-angle term will be ignored in this paper due to a poor signal-to-noise ratio in the far offsets.

If a rock mass has HTI symmetry, then the AVO gradient will behave as an ellipse with respect to compass direction (Rüger, 1998). Since the orientation of the symmetry axis is typically unknown and the terms B and D from Equation (6) are not easily decoupled, Jenner et al. (2001) organizes equation (6) for an offset-to-depth ratio < 1 as a function of the survey azimuth:

$$R_{pp}(\theta, \phi) \cong A + (b_{11}\cos^2\phi + 2b_{12}\cos\phi\sin\phi + b_{22}\sin^2\phi)\sin^2\theta, \quad (7)$$

where the coefficients b_{ij} define the general form of the AVO ellipse and whose angle (φ) and magnitude $G_{max,min}$ relative to the principle axis are given by:

$$\varphi = \tan^{-1} \left[\frac{b_{22}-b_{11} + ((b_{22}-b_{11})^2 + 4b_{12}^2)^{\frac{1}{2}}}{2b_{12}} \right], \quad (8)$$

$$G_{max,min} = \frac{1}{2} \left[b_{11} + b_{22} \pm ((b_{11} - b_{22})^2 + 4b_{12}^2)^{\frac{1}{2}} \right] \quad (9)$$

(after Jenner et al., 2001). The previous equations will provide the principle axes of the AVO ellipse without a 90-degree ambiguity only if the gradients do not change sign with azimuth (Rüger, 2002).

6.3 Data Preparation

The Dickman 3D is a vertical component survey with 3.3 mi² (8.5 km²) of coverage, 1.6 mi² (4.1 km²) of which is available for the AVAZ analysis (Figure 33). The data were acquired in 2001 along E-W receiver lines from an irregular shot grid. The bin spacing is 82.5 × 82.5 ft (25.1 × 25.1 m); however, the fold varies spatially due to the sporadic shot locations. Approximately 55000 prestack traces, which make up about a fifth of the original survey, are available for the analysis.

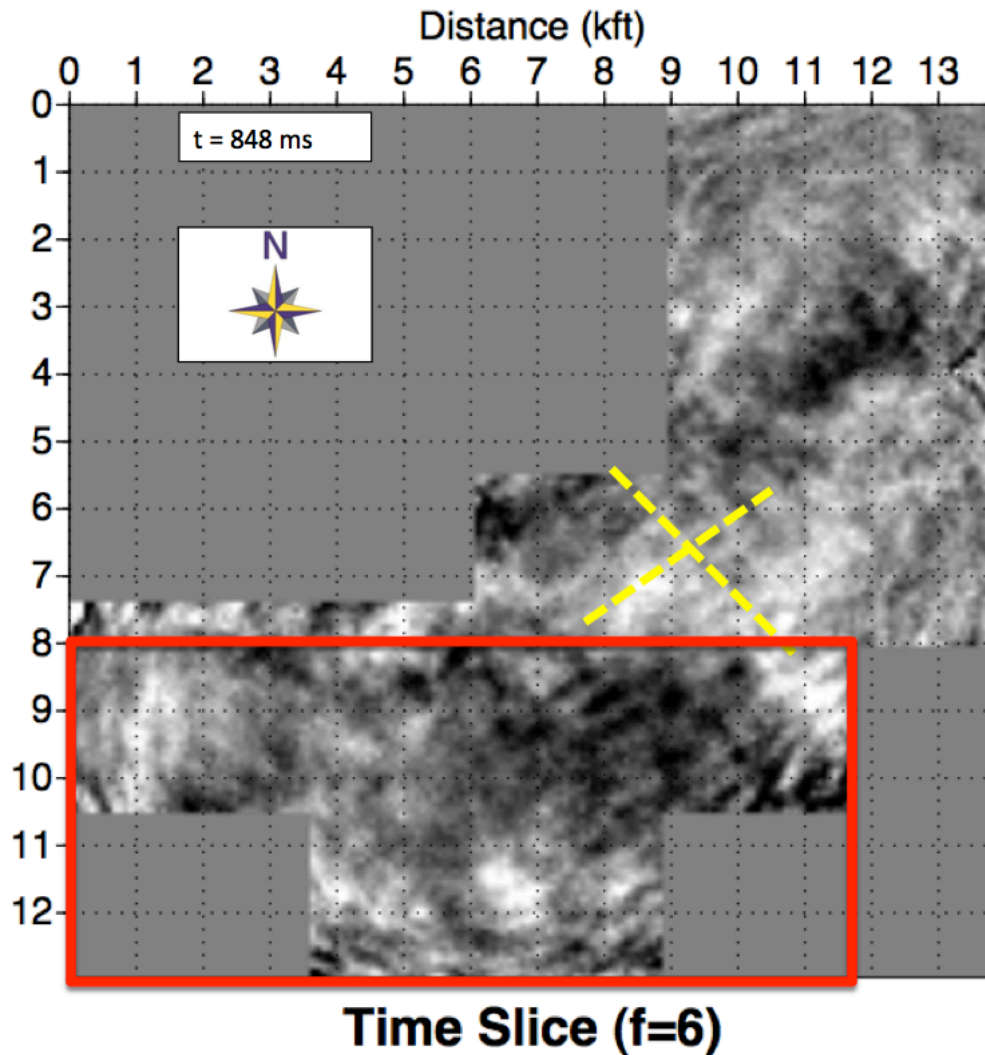


Figure 33: 6 Hz time slice (details previously discussed in Figures 4 and 15) showing seismic coverage and prestack coverage (Red Box).

Figure 34 shows a fold map with 82.5 ft (25.1 m) bin spacing. The maximum fold reaches about 100, which is insufficient for AVAZ analysis. Therefore, the CMP's were compiled into super-bins, thus increasing the fold and subsequently improving the azimuthal-offset coverage. Two opposing factors influence the choice of super-bin size: 1) a low azimuthal-offset fold resulting from too small of a bin size and 2) heterogeneity effects resulting from too large of a bin size. It can be seen from the

Dickman acquisition geometry that the CMP locations coalesce into north-south oriented clusters (Figure 35). Since these clusters generally span 300 to 500 ft (90 to 150 m in length, 400 ft (120 m) spacing was determined to be the optimal size (Figure 36).

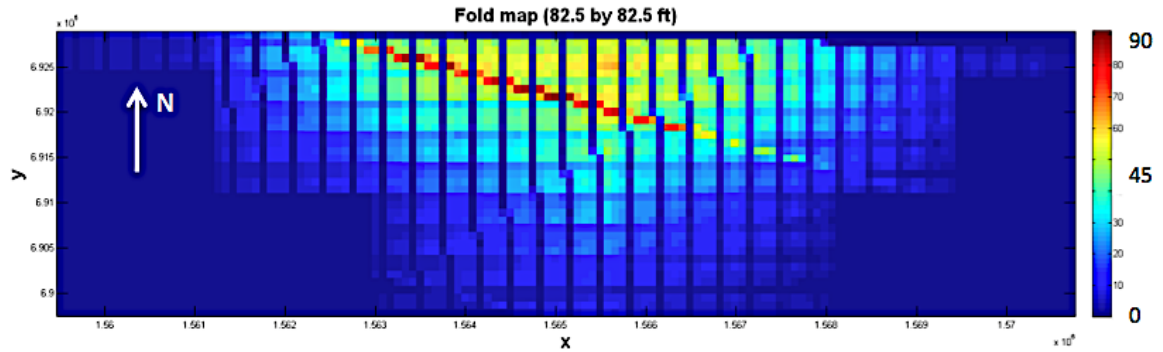


Figure 34: Fold map of the Dickman prestack coverage. Bin sizes are 82.5×82.5 ft (25.1×25.1 m) with warm colors representing the highest fold.

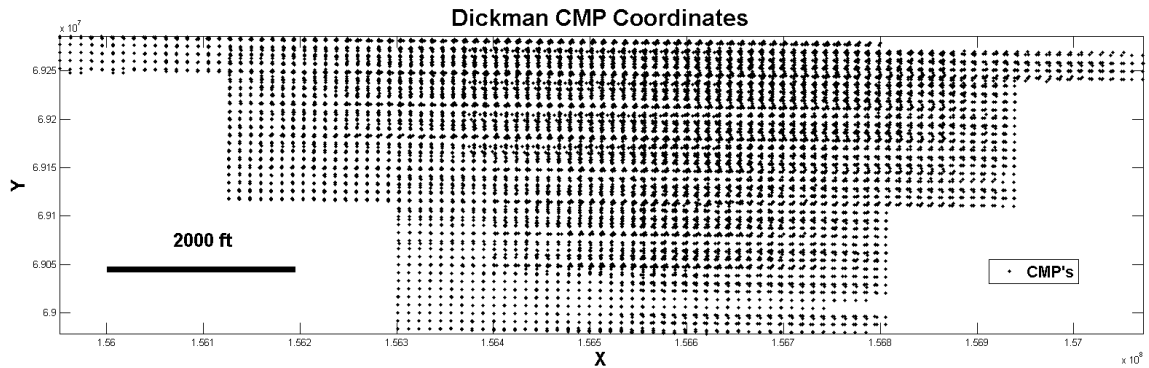


Figure 35: Dickman prestack CMP locations. Notice that the CMP locations coalesce into north south oriented clusters.

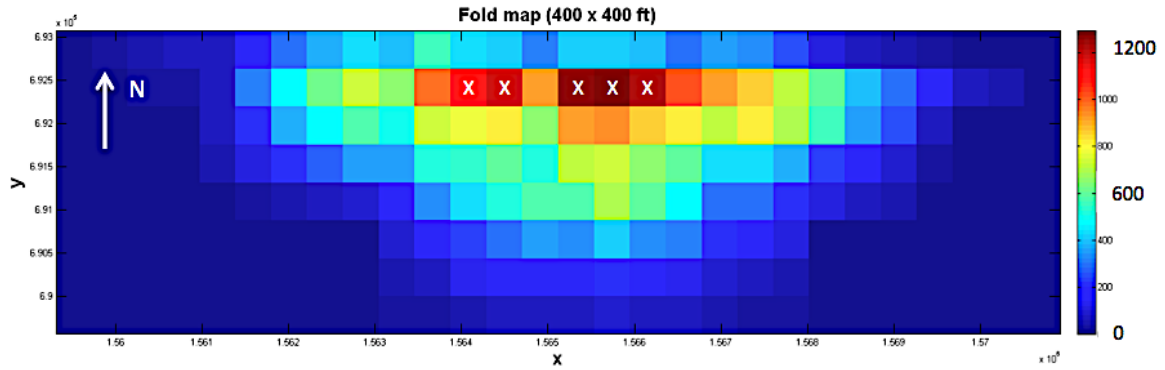


Figure 36: Fold map of the Dickman prestack coverage. Bin sizes are 400×400 ft (120×120 m) with the warm colors representing the highest fold. The X's mark the inversion bins.

Figure 37 describes the AVAZ inversion workflow. The overall goal in AVO processing is to preserve relative amplitude information. AVAZ processing takes a step further in that it also requires the preservation of relative azimuthal information; therefore, noise reduction techniques, multi-trace processes, as well as prestack migration algorithms commonly used in conventional AVO processing are generally avoided (Holmes and Thomsen, 2002). There are, however, methods such as those outlined by Gray et al. (2009), which incorporate more sophisticated algorithms into the AVAZ processing flow. Two noteworthy steps are the moveout-based anisotropic spreading correction (Xu and Tsvankin, 2006) and an azimuthally sensitive PSTM (Prestack Time Migration) of common offset vectors, which converts common mid-point gathers into a common reflection point gathers (Cary, 1999). These processes, however, were not incorporated into the Dickman processing flow.

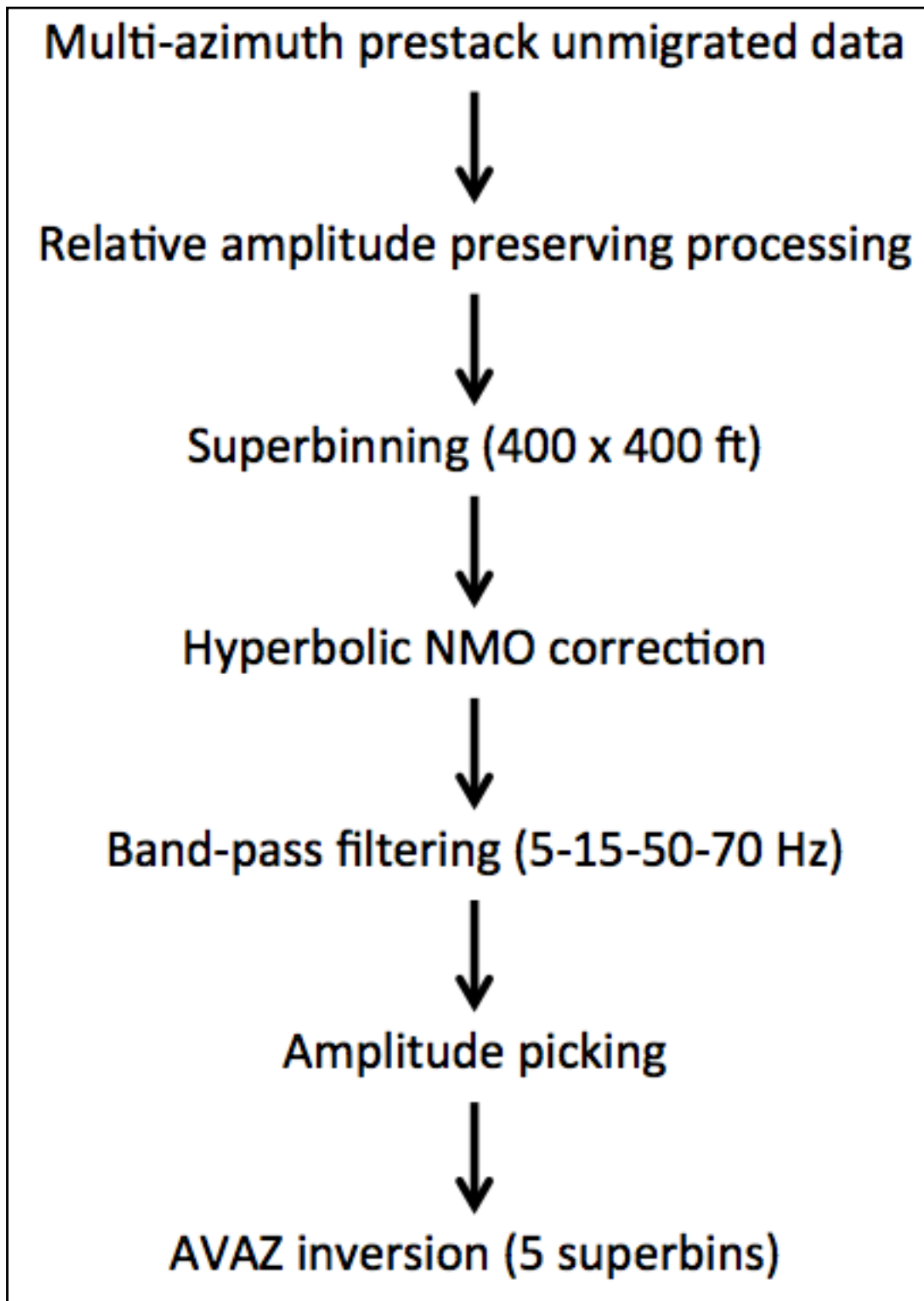


Figure 37: AVAZ inversion workflow.

The Dickman data was originally processed by Sterling Seismic Services LTD (2001) and then reprocessed in 2007 by the Allied Geophysical Laboratory (The University of Houston). The use of the data for AVAZ was not an objective in the original design of the processing flow. Since the raw gathers are not available, the dataset used in this analysis inherits a portion of the initial processing. The prior processing flow consisted of a statics correction, a time-gain function, surface consistent amplitude analysis, linear noise removal (primarily due to ground roll), and surface consistent deconvolution. From here, the standard hyperbolic normal-moveout (NMO) correction was applied to the super-gathers followed by a 1D band-pass filter (corner frequencies=5, 15, 50, and 70 Hz). The filter is designed to remove low and high frequency interference effects that have intrinsic frequency dependent azimuthal variations. The filter also improves event clarity (Figure 38).

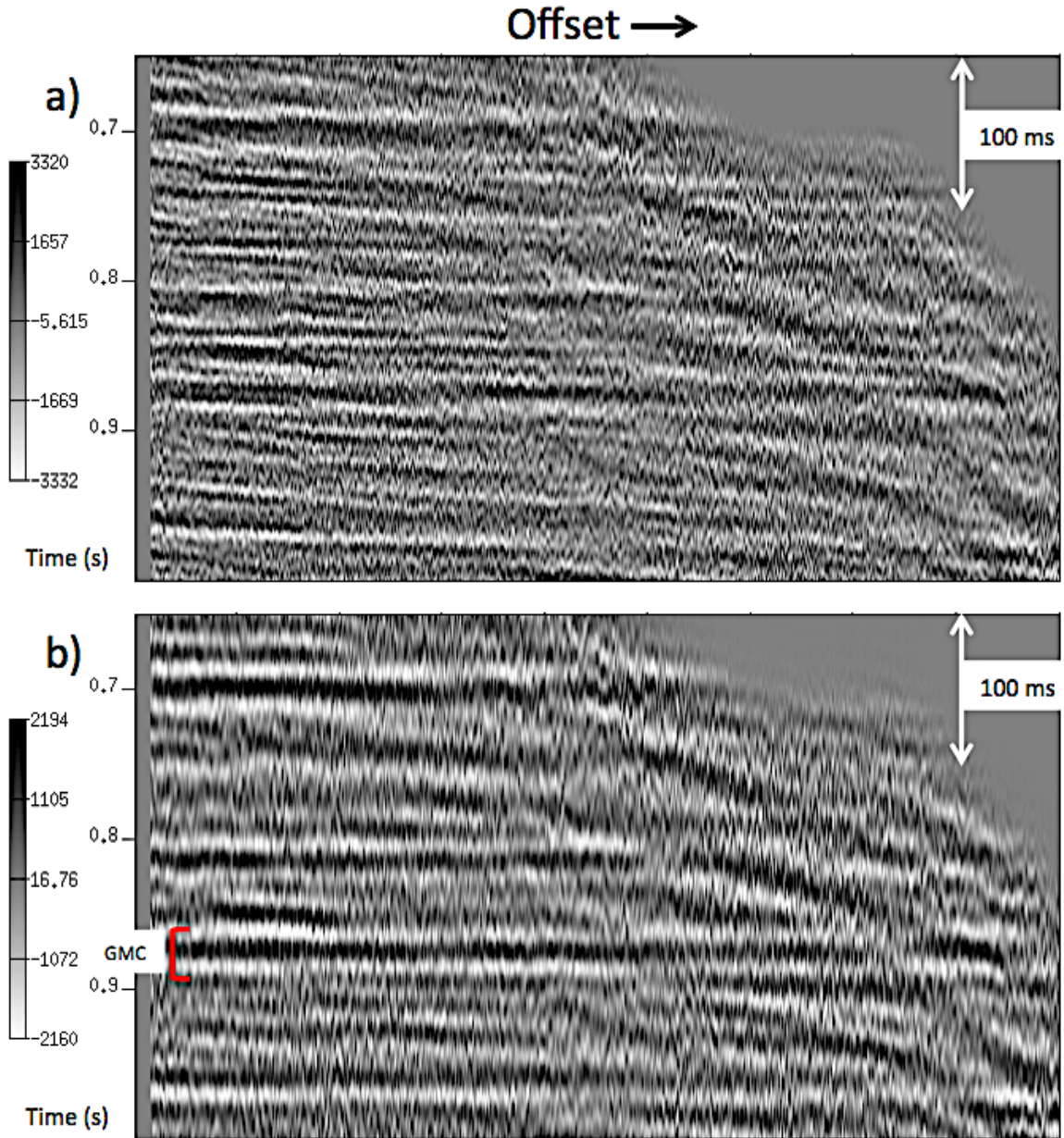


Figure 38: NMO corrected supergather before (a) and after (b) applying a zero-phase filter (corner frequencies: 5, 15, 50, and 70 Hz). Notice that reflectors are better resolved after applying the filter. The Gilmore City formation (GMC) is represented as a peak at about 875 ms. Notice the sloping events at far offsets. The AVAZ inversion ignores these far offsets and assumes an offset-depth ratio equal to 1.

The horizon of interest approximates the Osage/Gilmore City contact, which occurs around 875 ms as a peak in the super-gathers (Figure 38b). The maximum amplitude is picked in a 10 ms window centered on this horizon. The method of AVAZ inversion is that of Holmes and Thomsen (2002) and Hall and Kendall (2003). First, A (normal incidence P-wave reflection coefficient) from the two-term isotropic AVO Equation (5) is determined using a least-squares fit as in conventional AVO analysis. Then, keeping the normal-incidence value fixed, the least squares solution to the normal equations is used to find the coefficients b_{ij} from Equation (7). Equations (8) and (9) are used to find the rotation and magnitude of the AVO gradient ellipse. The results are plotted as a vector with an orientations determined by Equation (8). The length of the vector is taken as the difference between the major and minor axes normalized by the maximum ellipse magnitude calculated in this analysis.

6.4 Results

The AVAZ inversion is applied to 5 superbins and results are shown in Figure 39 (the results assume the 180 degree azimuthal equivalent). The orientation and magnitude of a particular AVO ellipse is represented as a vector with the origin at the center of the respective bin (Figure 39a). The rose diagram shows an average orientation of east-northeast ranging from 44 to 80 degrees relative to true north (Figure 39b). This lateral variation in vector orientation, as well as magnitude, is not surprising since the fold is relatively low when compared to the bin dimensions. Consequently, there likely exists a heterogeneity impact, which may create a spatial dependence for reflectivity, as opposed to an entirely azimuthal and offset dependency. Nevertheless, results show some degree of consistency in terms of azimuthal anisotropy orientation.

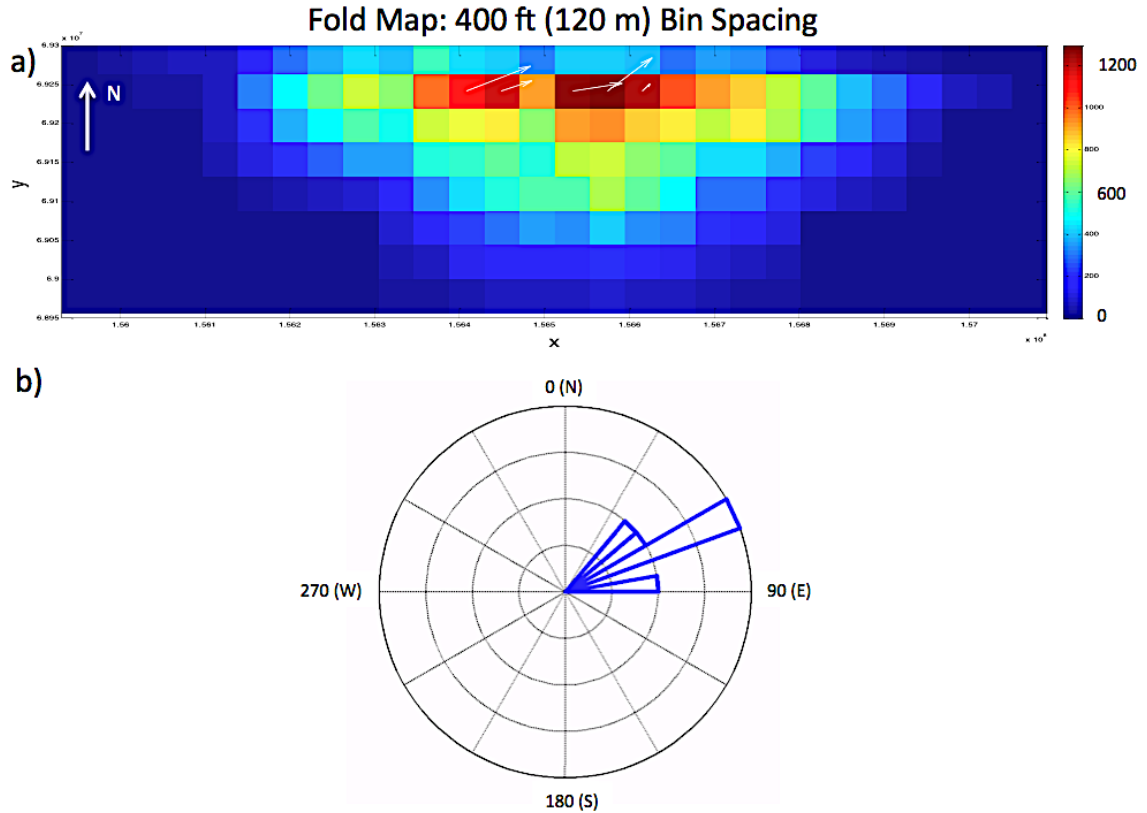


Figure 39: AVAZ inversion results superimposed on (a) 400 ft (120 m) fold map and (b) as a rose diagram. The results assume the 180 degree orientation equivalent. The average orientation is east-northeast ranging from 44 to 80 degrees relative to true north. The results assume the 180 degree azimuthal equivalent.

In order to make sense of the anisotropy magnitude as well as resolve the 90° ambiguity in orientation, AVAZ results are superimposed on an ANT Track volume extracted at the Gilmore City horizon (Figure 40). ANT Track is a post-stack seismic attribute developed by Schlumberger and is used to uncover subtle planar features, which are related to fracturing. The ANT Track lineaments by themselves appear chaotic in character, lacking any preferred orientation. If this is a dominant trait of the reservoir fracture network, then the calculated AVO ellipses should symbolize an anisotropy compromise to a more complicated symmetry, which

would be indeterminable by this AVAZ method. On the other hand, the three east-most vectors do tend align with an ANT Track feature, perhaps evidence of a sub-resolution fault (Figure 41); otherwise, there are no definitive correlations with other attribute features.

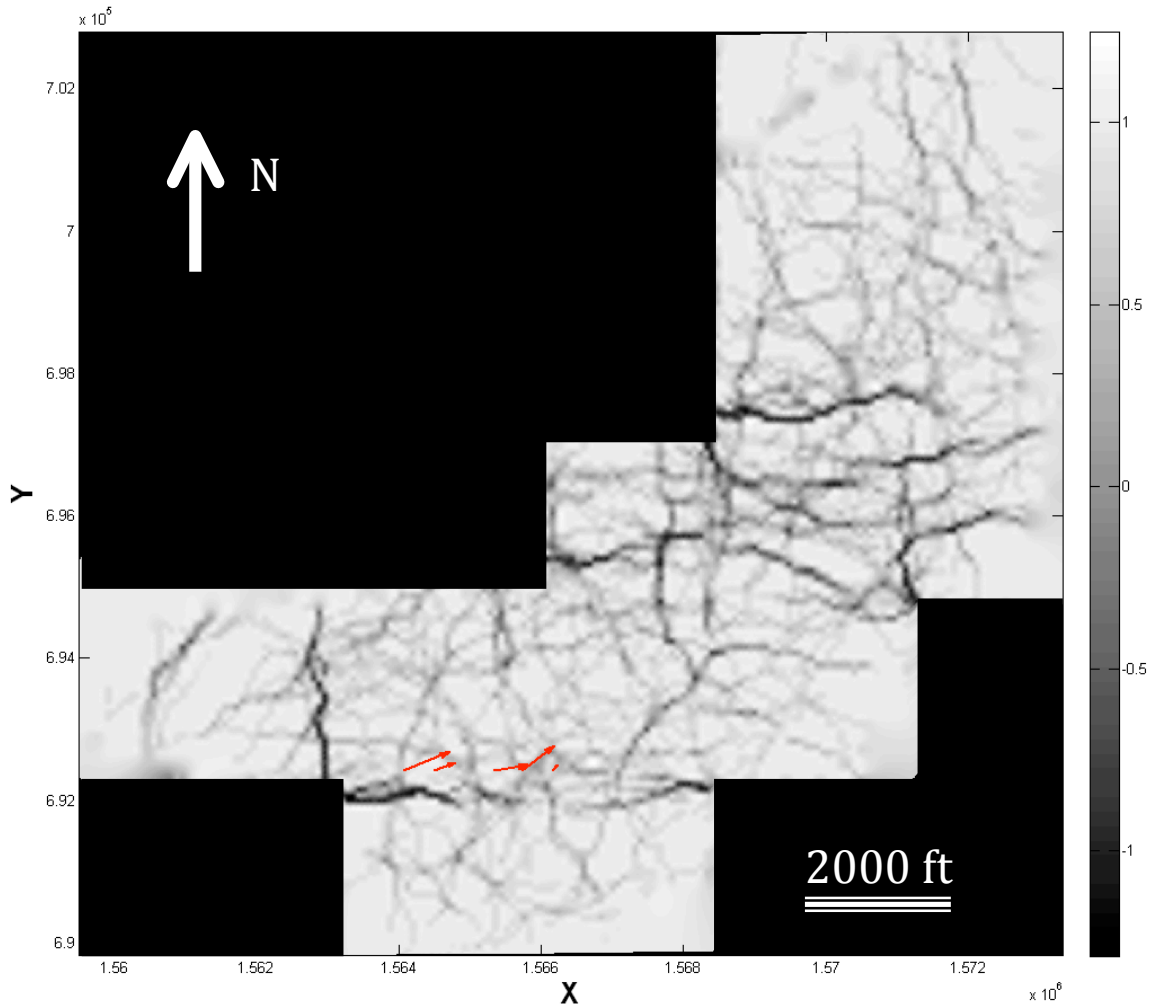


Figure 40: AVAZ inversion results plotted on an ANT Track volume extracted at the Gilmore City horizon. The ANT Track features show an erratic behavior lacking any preferred orientations.

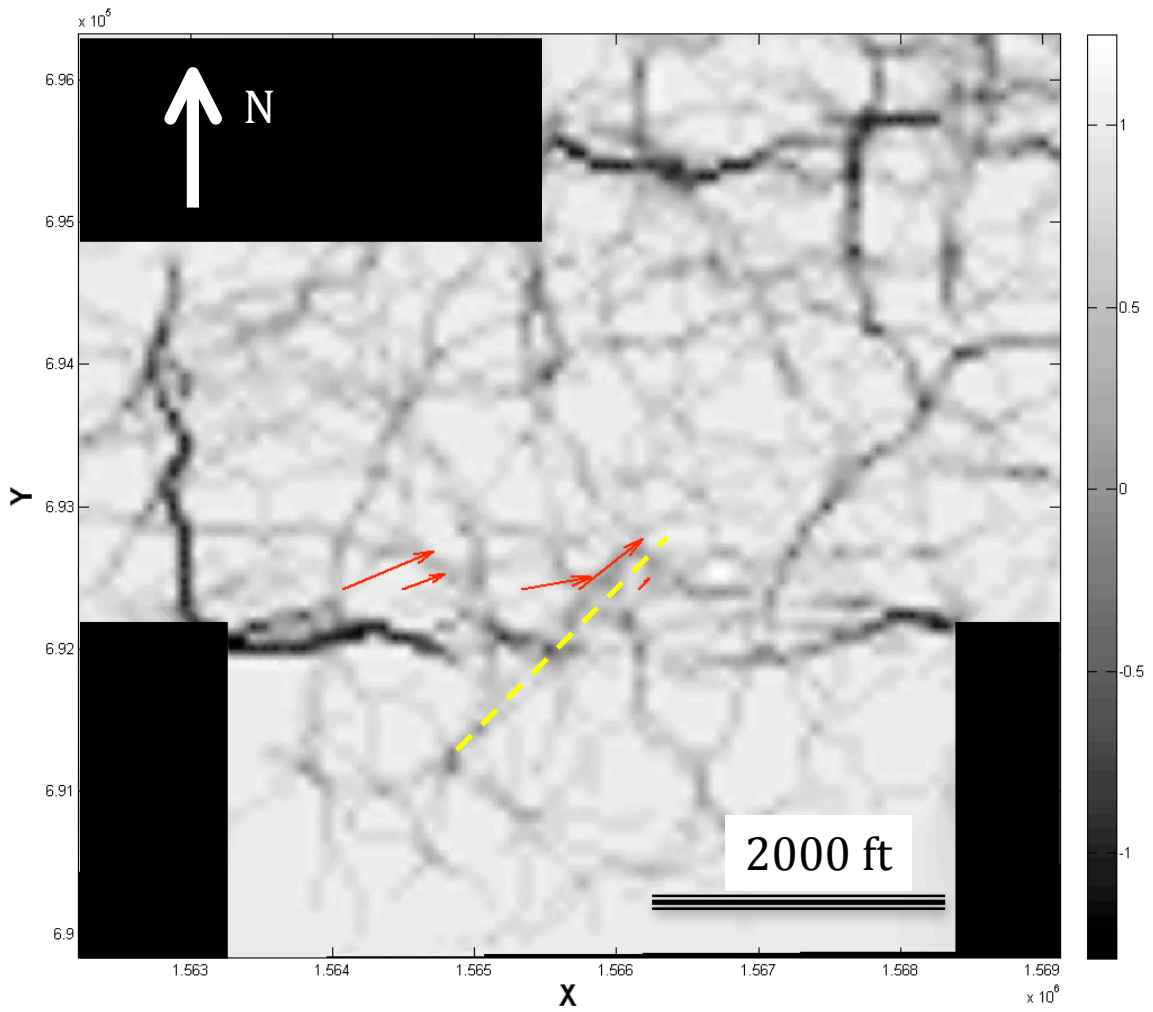


Figure 41: Zoomed in version of Figure 40. The two west-most vectors do not align with any ANT Track feature, with exception to the prominent one just to the south. The three east-most vectors do tend align with an ANT Track feature (dashed line), perhaps evidence of a sub-resolution fault

7.0 Discussion

A detailed characterization of natural fractures at the Dickman Field, in terms of understanding the spatial continuity and geometry, requires sufficient geologic and geophysical data. The available Dickman Field data are not entirely ideal for fracture characterization methods discussed in this work.

The FIS is limited two wells, which lack direct fracturing evidence. Therefore, interpreting the results becomes subjective. Moreover, the high-frequency log response character associated with fracturing is based on universal observation. When this empirical relationship is valid, fractures are prospectively detectable using a fuzzy inference system. However, since high-frequency log responses are not unique to fracturing, the FIS becomes sensitive to rapid lithology changes, pore fluid changes, and unstable tool behavior. For example, Figure 42 shows the FIS results for Sidebottom 6. The interval of interest was extended into 30 ft (9 m) of overlying Cherokee sandstone (Lower Pennsylvanian) to test the FIS response to a rapid lithology change. The largest FI value (0.45) occurs at 4390 ft (1338 m) MD, which approximates the unconformity and represents a sandstone-carbonate transition. The input logs characterize this lithology change as a rapid, or high frequency response on their respective curves. Without proper constraint, FI responses like these lead to fracturing misinterpretations. Consequently, this type of well log analysis is most apt for competent and homogenous rockmasses.

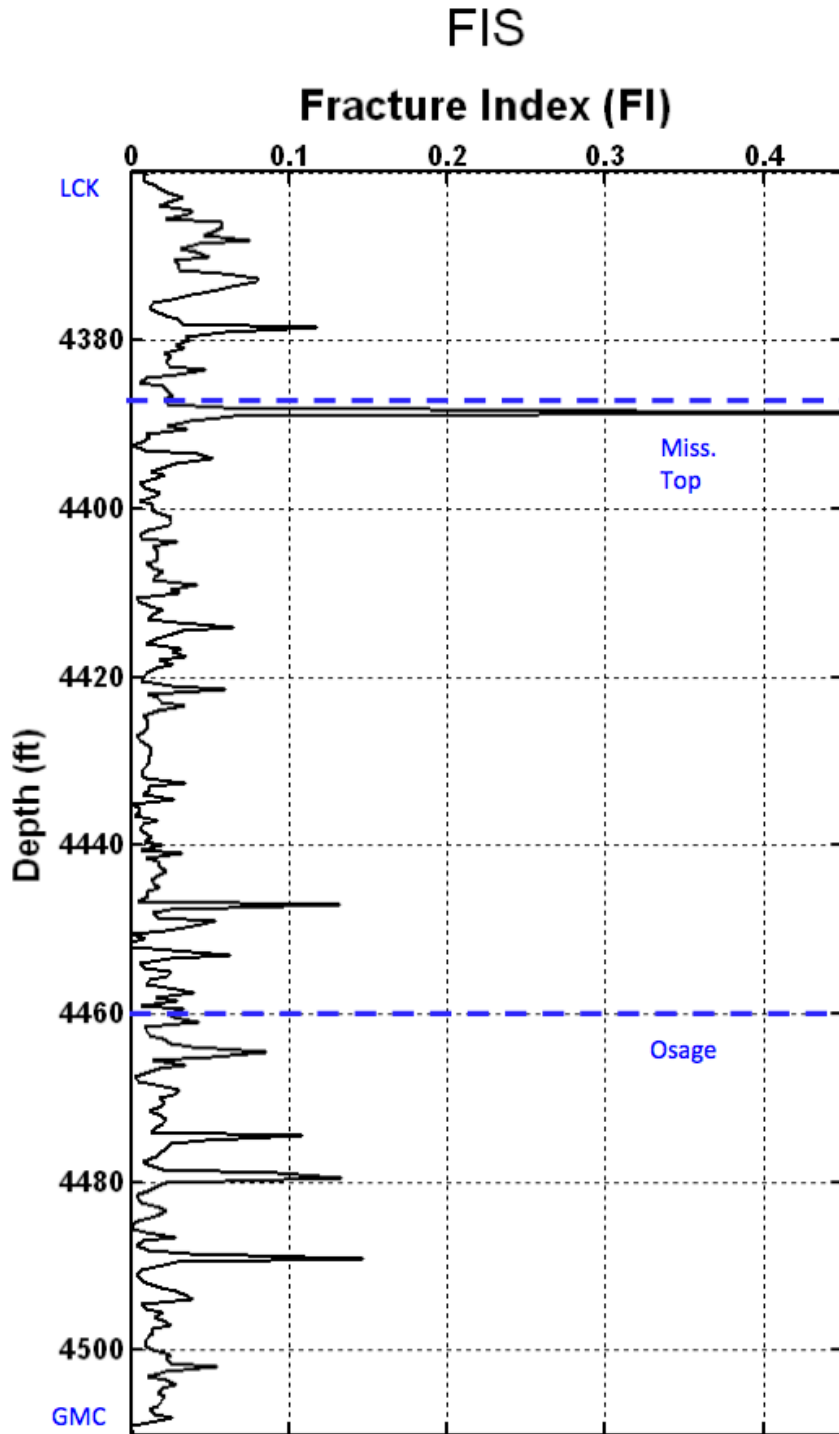


Figure 42: Sidebottom 6 FIS results. The depth scale is MD. The Mississippian formation top corresponds with the large FI value (0.45). This formation top describes a sandstone/limestone lithology change. This correlation describes the sensitivity of the FIS to rapid lithology changes.

The Dickman prestack seismic data suffers from poor spatial coverage and fold, which makes subsequent prestack inversion methods more susceptible to the heterogeneity influences from Mississippian stratigraphy. To begin with, the AVAZ inversion was limited to 5 superbins, which makes up less than a percent of the seismic coverage. The anisotropy information, as it pertains to principal stress orientations or fracture geometry, is therefore spatially constrained. Furthermore, the prominent channel features and collapse structures ubiquitous in the Dickman area (Figure 17 Section 4.0) likely cause waveform distortions via lateral velocity variations and transmission effects (Zheng et al., 2008); these effects are even more exaggerated by the superbining procedure. Moreover, the AVAZ model assumes a single set of parallel fractures. When this assumption is violated, the inversion results do not properly characterize the actual fracture geometry in the Mississippian reservoir interval. Therefore, inferring anisotropic information from the Gilmore City horizon becomes even more speculative.

However, reservoir studies with CO₂ sequestration implications should consider a similar fracture characterization approach. Assuming sufficient well log data and proper validation, the FIS analysis described in this work could extrapolate reservoir-fracturing characteristics to surrounding wellbores. If an effective medium model (i.e. HTI or Orthorhombic) amply describes the fracture geometry inferred from this borehole method, then AVAZ inversion could approximate the orientation of the in situ stress state of the reservoir. As a result, a more precise CO₂ flow simulation that also models directional fluid movement could be generated.

8.0 Conclusions

Carbon capture and storage programs are a viable solution for reducing anthropogenic CO₂ in the Earth's atmosphere. Because these programs consider geologic storage scenarios, proper characterization of reservoir properties is necessary. The Dickman Field serves as a research site for potential land-based CO₂ sequestration projects. A fracture characterization study of the target reservoir was carried out using available well logs and prestack seismic data.

The results from a low-frequency isolation filter (6 Hz) show NW and NE striking lineaments in the reservoir interval. Since these spectral anomalies may be related to noise in the upper 200 ms of the 3D volume, other fracture detection methods were considered.

A Fuzzy Inference System was designed to uncover fracture indicators from well logs assuming a high frequency response upon interaction with fractured rock. The result is a weighted summation of membership degrees, which reflect the fracture response character of the input logs. By evaluating all the logs in parallel, potential false positives were reduced in the output. Results show probable indicators of crosscutting fractures in the Mississippian section. However, a major limitation is the lack of concrete fracturing evidence required to validate the FIS results. Although not a robust method for the Dickman Field, the FIS analysis is a prospective fracture characterization method applicable to sites with sufficient borehole data.

AVAZ analysis detects azimuthal variations in the AVO gradient assuming a systematic set of fractures. When this assumption is valid, the AVO gradient will behave as an ellipse and the orientations of the major and minor axes will relate to the symmetry and isotropy planes of the HTI model. Results show comparable axes orientations (NNE) to the 6 Hz anomalies as well as with lineament orientations found in previous seismic attribute studies. These results indicate there is an underlying structural trend capable of being detected by seismic methods.

9.0 Future Work

Attempting to validate the FIS results from lithology strip logs was a major obstacle in this research. This application was severely limited due to the lack of direct fracture information from the examined wellbores. Therefore, future endeavors should incorporate borehole image logs or core data to calibrate the FIS. Fracture characteristics such as geometry (orientation and dip) and type (natural or drilling induced) could be defined from this information. Then, a neuro-fuzzy network (Roger et al., 1997) could be used to find the principal component logs most sensitive to fracturing, which would lead to a more accurate extrapolation to local wellbores.

References

- Carr, T. R., Merriam, D. F. and Bartley, J. D., 2005, Use of relational databases to evaluate regional petroleum accumulation, groundwater flow, and CO₂ sequestration in Kansas: AAPG Bulletin 89, no. 12, 1607–1627.
- Castagna, J. P., Sun, S. and Siegfried, R. W., 2003, Instantaneous spectral analysis: Detection of low-frequency shadows associated with hydrocarbons: *The Leading Edge*, 22, 120–127.
- Chen, H., Brown, R. L. and Castagna, J. P., 2005, AVO for one- and two-fracture set models, *Geophysics*: 70, 1-5.
- Connolly, P., 1999, Elastic impedance: *The Leading Edge*, 18, 438-452.
- Crain, E. R., Updated 2012, Crain's Petrophysical Handbook [online]: <http://www.spec2000.net/01-index.htm> (Accessed September-November, 2011).
- Davidson, H. C. de Coninck, Loos, M. and Meyer, L.A. (eds.), 2005, IPCC Special Report on Carbon Dioxide Capture and Storage: Cambridge University Press, Cambridge, United Kingdom and New York, NY.
- Demicco, R.V., and Klir, G. J. (eds.), 2004, *Fuzzy Logic in Geology*: Elsevier Academic Press, New York, NY.
- Franseen, E. K., Carr, T. R., Guy, W. J. and Beaty, S. D., 1998, Significance of depositional and early diagenetic controls on architecture of a karstic-overprinted Mississippian (Osagian) reservoir, Schaben field, Ness County, Kansas: AAPG, Annual Convention, Salt Lake City, Extended Abstracts, v. 1, A210-A214.
- Global CCS Institute, 2011, The global status of CCS: Global CCS Institute, Canberra, Australia [online]: www.globalccsinstitute.com/resources/publications/global-status-ccs-2010 [Accessed August-September 2011].
- Gray, D., Schmidt, D., Nagarajappa, N., Ursenbach, C., and Downtown, J., 2009, An azimuthal-AVO-compliant 3D land seismic processing flow: Canadian Society of Exploration Geophysicists, Expanded Abstracts.
- Hall, S., and Kendall, J. M., 2003, Fracture characterization at Valhall: Application of P-wave amplitude variation with offset and azimuth (AVOA) analysis to a 3-D ocean-bottom data set: *Geophysics*, 68, 1150-1160.

Hilterman, F. J., 2001, Seismic Amplitude Interpretation, 2001 Distinguished Instructor Short Course, Distinguished Instructor Series, No. 4, Soc. Expl. Geophysics.

Jenner, E., Williams, M. and Davis, T., 2001, A new method for azimuthal velocity analysis and application to a 3D survey, Weyburn field, Saskatchewan, Canada: 71st Annual International Meeting, Society of Exploration Geophysicists, Expanded Abstracts, 102-105.

Jorgensen, D. G., Helgesen, J. O., and Imes J. L., 1993, Regional Aquifers in Kansas, Nebraska, and Parts of Arkansas, Colorado, Missouri, New Mexico, Oklahoma, South Dakota, Texas, and Wyoming - Geohydrologic Framework: U.S. Geological Survey Professional Paper 1414-B, 72 p.

Kruger, J. M., 1997, On-line gravity and magnetic maps of Kansas: Kansas Geological Survey Open-File Reports 96-51 and 97-72:
<http://www.kgs.ku.edu/PRS/PotenFld/potential.html> (Accessed August-September, 2011).

Liner, C., Zeng, J., Geng, P., King, H., Li, J., Califf, J. and Seales, J., 2010, 3D seismic attributes and CO₂ sequestration: DOE Final Report

Liu, E., Zelewski, G., Lu, C., Reilly, R. M. and Shevchek, Z. J., 2011, Mitigation of overburden effects in fracture prediction using azimuthal AVO analysis: An example from a Middle East Carbonate field: *The Leading Edge*, 30, no. 9, 750-756.

Martinez, L., Gupta, A. and Brown, R., Interpretation of Important Fracture Characteristics from Conventional Well Logs, SPE paper 67280 Presented at the Production and Operations Symposium, 25- 28 March, 2001, Oklahoma City, OK.

Mathworks, 2006, Fuzzy Logic Toolbox User's Guide: Mathworks Inc.

Merriam, D., 1963, Geologic History of Kansas: Kansas Geological Survey Bulletin 162 [online]: http://www.kgs.ku.edu/Publications/Bulletins/162/08_patt.html (Accessed August-October, 2011).

Nelson, R. A., 2001, Geological Analysis of Naturally Fractured Reservoirs: Gulf Publishing Company, Houston, TX.

Nissen, S. E., Carr, T. R. and Marfurt, K. J., and Sullivan, E. C., 2009, Using 3-D seismic volumetric curvature attribute to identify fracture trends in a depleted Mississippian carbonate reservoir: implications for assessing candidates for CO₂ sequestration: *AAPG Studies in Geology* 59, 297-319.

- Partyka, G. A., Gridley, J. A., and Lopez, J. A., 1999, Interpretational aspects of spectral decomposition in reservoir characterization: *The Leading Edge*, 18, 353–360.
- Plasynski, S., Deel, D., Miller, L. and Kane, B., 2007, Carbon sequestration technology roadmap and program plan: U.S. Department of Energy, Office of Fossil Energy, National Energy Technology Laboratory, e-report.
- Puryear, C. I., Portniaguine, O. N., Cobos, C., and Castagna, J. P., in press, Constrained least squares spectral analysis: Application to seismic data: *Geophysics*.
- Roger, J. S., Sun, C. T. and Mizutani, E., *Neuro-Fuzzy and Soft Computing*: Prentice Hall, Upper Saddle River, NJ, 1997.
- Rüger, A., 1998, Variation of P-wave reflectivity with offset and azimuth in anisotropic media: *Geophysics*, 63, 935–947.
- Rüger, A., 2002, Reflection Coefficients and Azimuthal AVO Analysis in Anisotropic Media: Society of Exploration Geophysicists.
- Seales, J., Brown, T., and Liner, C., 2011, Channel and fracture indicators from narrow-band decomposition at Dickman field, Kansas: *SEG Expanded Abstracts* 30, 1830.
- Shuey, R., 1985, A simplification of the Zoeppritz equations: *Geophysics*, 50, 609-614.
- Thomsen, L., 1986, Weak elastic anisotropy: *Geophysics*, 51, 1954-1966.
- Thomsen, L., 1995, Elastic anisotropy due to aligned cracks in porous rock: *Geophys. Prosp.*, 43, 805-829.
- Tsvankin, I., 1997, Anisotropic parameters and P-wave velocity for orthorhombic media: *Geophysics*, 62, 1292-1309.
- Twiss, R. J., and Moores, E. M., 2006, *Structural Geology*: W. H. Freeman.
- Xu, X., and Tsvankin, I., 2006, Anisotropic geometrical-spreading correction for wide-azimuth P-wave reflections: *Geophysics*, 71, no. 5, 161-170.
- Yilmaz, I., 2001, *Seismic Data Analysis*: Society of Exploration Geophysicists.
- Zheng, Y., Wang, J., and Perez M., 2008, Pitfalls and tips for seismic fracture analysis: 78th Annual International Meeting, SEG, Expanded Abstracts, 1531-1535.

Ziegler, P. A., 1989, *Evolution of Laurussia*, Dordrecht, The Netherlands, Kluwer Academic Publishers, 102 pp.

Appendix A

MATLAB Information:

Version 7.10.0

Fuzzy Logic Toolbox Version V2.2.11 (R2010a)

